Characteristics of Mars UV dayglow emissions from atomic oxygen at 130.4 and 135.6 nm: MAVEN/IUVS limb observations and modeling

B. Ritter[1,2,*], J.-C. Gérard[1], L. Gkouvelis[1], B. Hubert[1], S. K. Jain[3], N. M. Schneider[3]

[1] LPAP, STAR Institute, Université de Liège, Belgium

[2] Royal Observatory of Belgium, Brussels, Belgium

[3] LASP, University of Colorado, USA

[*] Corresponding author: Birgit Ritter (b.ritter@uliege.be)

May 2019

Keypoints

1. Two Martian years of UV dayglow limb observations of oxygen at 130.4 and 135.6 nm; first published results at 135.6 nm since Mariner 6/7.
2. Solar flux cannot fully explain the brightness variations; strong correlation of the emissions confirms current photochemistry understanding.
3. Emissions mainly arise from direct excitation of O; limb brightness and peak altitude are strongly modulated by CO_2 absorption.

Abstract

We present an overview of two Martian years oxygen dayglow limb observations of the ultraviolet (UV) emissions at 130.4 nm and 135.6 nm. The data have been collected with the IUVS instrument on board the MAVEN spacecraft. We use solar flux measurements of EUVM on board MAVEN to remove the solar induced variation and show the variations of the maximum limb brightness and altitude with season, SZA and latitude, which reflects the strong variability of the Martian atmosphere. The 130.4 and 135.6 nm peak brightness and altitudes are strongly correlated and behave similarly. Both emissions are modeled for selected data using Monte Carlo codes to calculate emissions arising from electron impact on O and CO_2. Additional radiative transfer calculations are made to analyze the optically thick 130.4 nm emission. Model atmospheres from the Mars Climate Database serve as input. Both simulated limb profiles are in good agreement with the observations despite some deviations. We furthermore show that the observed 130.4 nm brightness is dominated by resonance scattering of the solar multiplet with a contribution (15-20%) by electron impact on O. Over 95% of the excitation at 135.6 nm arises from electron impact on O. Simulations indicate that the limb brightness is dependent on the oxygen and CO_2 content, while the peak emission altitude is mainly driven by the CO_2 content because of absorption processes. We deduce $[O]/[CO_2]$ mixing ratios of 3.1% and 3.0% at 130 km for datasets collected at L_S=350° in Martian years 32 and 33.

1 Introduction

The lower Martian atmosphere consists mainly of CO_2 (e.g. Nier and McElroy, 1977) with minor contributions of argon, N_2, O_2 and CO. Traces of other species are also present. In the thermosphere, the highly dynamical intermediate region between the lower atmosphere and the induced magnetosphere (Bougher et al., 2000), the composition is also governed by photochemical reactions producing and destroying neutral species and ions. One of them is neutral atomic oxygen that is produced by photodissociation of CO_2 (e.g. Barth, 1974) and which supersedes CO_2 as the most abundant neutral species above 200 km and up to the lower exosphere. Already since Mariner 4 radio occultation observations in 1965 atomic oxygen is known to be a minor constituent in the lower atmosphere (e.g. Donahue, 1966; McElroy, 1967), where it nevertheless plays a major role in the control of the thermal structure, also in the CO_2 dominated region. It contributes to highly efficient cooling of the Martian atmosphere through collisions with CO_2 molecules that are hence left in an excited vibrational state and dissipate their energy through the 15-µm thermal emission (Bougher and Roble, 1991, Bougher et al., 2014).

The first in situ mass spectrometer observations of the Martian atmosphere have been performed by the two Viking landers in 1976 (Nier and McElroy, 1977) that gave insight into the composition of the atmosphere. Quantitative analysis of atomic oxygen could, however, not be performed as oxygen is a highly reactive species and prone to possible recombination with the instrument surfaces. The Neutral Gas and Ion Mass Spectrometer (NGIMS; Mahaffy et al., 2015) onboard the Mars Atmosphere and Volatiles EvolutioN (MAVEN; Jakosky et al., 2015) now performs routine in situ density measurements down to 145 km in the atmosphere and even down to about 120 km during 'Deep Dip' campaigns of the mission (e.g. Bougher et al., 2017). [O]/[CO_2] mixing ratios between 2.2% and 3% at the lowest measured altitudes have been found on the dayside (Stone et al., 2018). Still, the derived oxygen densities have an uncertainty of a factor of 2 due to surface recombination processes (Fox et al., 2017). Oxygen densities have also been derived by photochemical equilibrium calculations using observations of O^+ from Viking measurements and electron temperature and density profiles. Hanson et al. (1977) derive an O mixing ratio of 1.5% at

130 km. Based on photochemical equilibrium calculations of CO_2^+, Fox and Dalgarno (1979) find ratios of 1.4% at 120 km and 3% at 130 km. Fox et al. (2017) compare an updated model with NGIMS 'Deep Dip' measurements and find model-derived atomic oxygen densities larger by a factor of 4 compared to the mass spectrometer results below 155 km. They use photochemical equilibrium calculations of O_2^+ and state that their model's main uncertainty is the electron density.

In contrast to in situ observations with mass spectrometers, observation of airglow of the respective atmospheric constituents with imaging spectrometers is a powerful tool to probe the atmosphere of a planet with a significant better coverage and down to lower altitudes. Limb observation of airglow emissions is a standard technique to study altitude profiles of the chemical species in the atmosphere and its thermal structures and allow observations at altitudes below the spacecraft periapsis. Emissions from excited O(^{1}S), O(^{3}S) and O(^{5}S) states of atomic oxygen fall into the ultraviolet (UV) range of the dayglow emission spectrum at 297.2, 130.4 and 135.6 nm respectively. While the O(^{1}S) state is largely produced by CO_2 dissociation and an exclusive indicator of the CO_2 density in the lower thermosphere (~70 km; Gkouvelis et al., 2018), the O(^{3}S) and O(^{5}S) state are expected to be good proxies of the oxygen content in the thermosphere (Strickland et al., 1972; Stewart et al., 1992). Limb profiles from the latter two excited states show peak brightness in the thermosphere between 100 and 150 km.

The first observations of the 130.4 and 135.6 nm multiplets were performed with UV spectrometers during the Mariner 6 and 7 flybys in 1969 and analyzed by Barth (1971), Thomas (1971), Stewart (1972) and Strickland et al. (1972). They found that resonance scattering of the solar multiplet is the main contributor to the 130.4 nm resonance triplet and that the 135.6 nm line doublet is mainly produced by photodissociation of CO_2, while Thomas (1971) concluded that it is mainly produced by photoelectron impact on atomic oxygen. They furthermore indicate that oxygen densities can be directly derived from the 130.4 nm data under the assumption of a given exospheric temperature plus a given solar flux at 130.4 nm and derived atomic oxygen mixing ratio of 0.5 to 1% at 135 km. To our knowledge, these are also the only reported results of 135.6 nm observations in the Martian atmosphere up to now. Afterwards, observations at 130.4 nm were reported also from

Mariner 9 (Strickland et al., 1973; Barth, 1974) that orbited Mars from November 1971 until October 1972. From these data, Strickland et al. (1973) deduced oxygen mixing ratios between 0.5 and 1% at 135 km. From the comparison of all Mariner data they expect that a variation of the oxygen density by a factor of 3 or more is not unexpected.

The UV channel of the SPICAM instrument on board Mars Express observed Mars between 2004 and 2011 and detected the weak signature at 135.6 nm, but no analysis was published. Leblanc et al. (2006) reported a dependence of the 130.4 nm triplet brightness and therefore of the oxygen density on the solar zenith angle (SZA), indicating a drop of oxygen density in the Martian atmosphere by an order of magnitude from SZA interval 14°-37° to 37°-60°. Chaufray et al. (2009) reported a decrease in the oxygen density by a factor of 2 between the SZA intervals 20°-55° and 55°-90° from SPICAM observations. Furthermore, they deduced an oxygen mixing ratio between 0.6 and 1.2%.

With the arrival of the Mars Atmosphere and Volatile EvolutioN (MAVEN) spacecraft at Mars in 2014 a new era of quasi-continuous airglow observations has begun. At the time of writing, two full Martian years of data are available covering a large part of the declining phase of solar cycle 24. The observations encompass various ranges of latitudes and SZA for the different epochs, providing a much more complete picture of the behavior of the planet's atmosphere than ever before. Among other scientific instruments, MAVEN carries the Imaging Ultraviolet Spectrograph (IUVS, McClintock et al., 2015) that collects spectra in in the range of 120-340 nm, and the Extreme Ultraviolet Monitor (EUVM, Eparvier et al., 2015). For the first time, the EUV solar flux is observed while UV dayglow measurements are being taken, which are driven by the solar flux. Chaufray et al. (2015) presented first results of 130.4 nm line limb observations from IUVS and used the data to derive atomic oxygen density in the range of 10^7–10^8 cm^{-3} for temperatures of 200–300 K at an altitude of 200 km using radiative transfer modeling.

In the present study, we investigate dayglow limb observations of the oxygen FUV emission multiplets at 130.4 and 135.6 nm by the IUVS instrument and take advantage of the simultaneous observations of the solar input by EUVM. The limb dayside observations range from $L_S = 217°$ in Martian Year (MY) 32 to $L_S = 192°$ in MY 34. Due to MAVEN's orbit around Mars and alternating operational modes, there is not continuous coverage of the dayside and neither continuous limb observations, but IUVS still provides an unprecedented and extremely rich dataset.

1.1 Emissions from the O(^{3}S) and O(^{5}S) excited states

The OI $^3S^0$–^3P transition is an allowed triplet-triplet transition to the ground state emitting at 130.22, 130.49 and 130.60 nm (here referred to as the 130.4 nm line). As it is an allowed transition to the ^3P ground state, it is subject to strong resonance scattering, and in particular the solar 130.4 nm triplet radiation is efficiently scattered (Equation (1)). Hence, the Martian atmosphere is optically thick at this wavelength, which requires the use of radiative transfer codes to account for multiple scattering in order to interpret the observations and link its brightness to the O abundance. Apart from solar irradiation, the O(^{3}S) state can be excited by direct electron impact on oxygen atoms (Equation (2)) and by electron dissociation of CO_2 (Equation (3)), CO and O_2 that leave a neutral oxygen atom in the excited state. Resonance scattering is clearly identified as the major contributor to this emission and other sources play a less important role. Electron impact on CO and especially on O_2 can be totally neglected. Even though electron impact on O and CO_2 are often neglected as minor sources, these sources now appear to contribute about 15-20% to the total observed emission rate as will be shown in this study. From those two process, electron impact on O is the dominant source above ~110 km. Quenching processes plays no role, as the radiative lifetime of the upper level of the transition is very short, in the order of 10^{-8} s.

$$h\nu_{130.4} + O \rightarrow O(^3S) \quad (1)$$

$$e^- + O \rightarrow O(^3S) + e^- \quad (2)$$

$$e^- + CO_2 \rightarrow CO + O(^3S) + e^- \quad (3)$$

The OI $^5S^0$–^3P transition is a forbidden quintet-triplet transition to the ground state at 135.56 and 135.85 nm (referred to as 135.6 nm line) and features no resonance scattering. It can be considered optically thin at Mars. The transition is weakly metastable (185 µs, Mason 1990) and therefore does not experience significant quenching at the low pressure levels of the Martian thermosphere. Possible sources are the same as at 130.4 nm, except for resonance scattering of the solar radiation: electron impact on O (Equation (4)) and electron dissociation of CO_2 (Equation (5)), CO and O_2. We will show that – following an update of excitation cross sections and modeling – the major source for this emission is indeed photoelectron impact on O while dissociative excitation of CO_2 by electron impact remains a minor source. Electron impact on CO and O_2 are neglected. Therefore, the produced 135.6 nm emission should be a direct indicator of the oxygen density in the Martian thermosphere.

$$e^- + O \quad -> \quad O(^5S) + e^- \qquad (4)$$

$$e^- + CO_2 \quad -> \quad CO + O(^5S) + e^- \qquad (5)$$

Photodissociation of CO_2 and CO by EUV solar radiation can lead to the production of oxygen atoms in the $O(^3S)$ and $O(^5S)$ excited states, but their contribution are expected to be negligible. Only upper limits of cross sections for the production of $O(^3S)$ are known that are in the order of 10^{-20} cm^2 at short wavelengths (Gentieu and Mentall, 1973).

Figure 1(a) shows a spectrum of the FUV channel of IUVS featuring the oxygen emissions. Other prominent features in the figure are for example the dominant Lyman-α line at 121.6 nm, atomic carbon lines at 127.8, 156.1 and 165.7 nm, a CII line at 133.5 nm and several lines of the CO 4th Positive bands. A more complete list can be found e.g. in Ajello et al. (2019). Figure 1(b) displays the corresponding limb profiles of the 130.4 nm (blue) and 135.6 nm (red) emissions. The dots indicate the maximum brightness of each profile.

2 Observations

The MAVEN spacecraft (Jakosky et al., 2015) orbits Mars on a highly elliptic trajectory in a 4.5-hour near-polar orbit with an inclination of 75°. The apoapsis altitude is 6250 km and the periapsis altitude flybys ~160 km. IUVS is one of the eight scientific instruments on board the spacecraft.

2.1 IUVS observations

IUVS on board MAVEN is capable of observing the Martian upper atmosphere within a total spectral range of 115–340 nm. This spectral range is divided into a far- and a mid-ultraviolet (FUV and MUV) channel. The oxygen emissions at 130.4 and 135.5 nm fall into the range of the FUV channel. The uncertainty of the absolute calibration in the FUV channel is currently estimated to ±25% (Jain et al., 2015). The spectral resolution of the FUV channel is ~0.6 nm, therefore the two oxygen multiplets are not resolved in this instrument mode. The echelle channel of IUVS is in principle able to separate the components in the two multiplets and the study of the individual line components will be exciting future work.

IUVS operates in limb, coronal scan, and disc modes, depending on the orbital phase. Here, we consider limb observations that cover tangent point (TP) altitudes between 70 and 200 km. The instrument is located on a two-axes gimbal and is equipped with a pivoting plane mirror that allows scanning and mapping as well as to chose between two different fields of regard ('limb' and 'nadir'). The combination of those allows the instrument to observe with a duty cycle of 50-100%, even though the respective spacecraft pointing requirements of the other instruments onboard MAVEN are normally not compatible with each other. The entrance slit of the instrument is 11° × 0.06° providing thereby the instrument field of view. The IUVS array detectors record images that contain spatial information in one and spectral information in the other dimension. In limb mode, the entrance slit is parallel to the orbit plane and to the direction of the spacecraft motion. The mirror reflects the incoming UV light onto the detectors before it rotates to point the field of regard to a different tangent point altitude in order to record the next spectral-spatial image. One periapsis limb scan is normally built up of 21 of these images and up to 12 individual limb scans can be taken per orbit. The cadence of the observations in limb mode is 4.8 seconds, with the integration and read-out time being of 4.2 and 0.6 seconds, respectively.

The IUVS instrumental team provides different levels of data products on the NASA Planetary Data System (PDS): Level 1A (raw data), level 1B (calibrated data), and level 1C (processed data). The processed data provides calibrated brightness of individual emission lines that are obtained through multiple linear regression fits of individual spectral components that had been identified in laboratory spectra and taking into account the reflected solar spectrum background (Stevens et al., 2011). The level 1C radiances are binned onto a defined TP altitude grid with a vertical resolution of 5 km. The IUVS FUV spectrum shown in Figure 1(a) is the average of 19 individual limb observations, recorded with tangent point altitudes between 120-140 km above the Martian surface.

2.2 EUVM observations

EUVM on board MAVEN continuously measures the solar EUV flux at Mars using three different wavelength channels: 0-7 nm, 17-22 nm, and 117-125 nm. From this data the full solar EUV spectrum is reconstructed (Thiemann et al., 2017) and 1 nm resolution spectra from 0-190 nm are available on the NASA PDS, for each minute as well as daily averaged spectra. The total solar 130.4 nm triplet radiance can be extracted from these spectra under some assumptions and can be employed for modeling (Section 4). We use EUVM model data Version 11.

2.3 Description of IUVS dataset

At the time of writing, the observations cover almost two full Martian years and provide an unprecedented dataset, covering various latitude ranges per epoch. The observations cover the time period from October 2014 till June 2018 corresponding to Southern summer in MY 32 till Southern summer of MY 34. The data used in this study is level 1C version 07 and 13. In Figure 1(b) several limb profiles at 130.4 nm (blue) and 135.6 nm (red) are plotted. A dot indicates the peak intensity between 100 and 170 km of each profile. In the following, mostly this peak intensity and the corresponding TP altitude (in the following only referred to as altitude) are used for analysis.

Note that for the optically thin 135.6 nm profile, the brightness peak altitude is a good approximation for the peak of the actual emission rate, the profile resembles a Chapman layer and the scale heights are relatively small. On the other hand, at 130.4 nm, the atmosphere is optically thick, meaning that the instrument observes the optically thick source function, which is attenuated exponentially by the scattering of the oxygen atoms and also by the absorption of CO_2. The observer does not see much farther than a distance corresponding to unity optical depth ($\tau = 1$), hence the observed brightness peak and its altitudes are more spread than at 135.6 nm. Also the topside scale height is significantly larger. The brightness at 135.6 nm is generally lower than at 130.4 nm, but the altitude of the peak emissions is comparable.

Figure 2 gives an overview of the available periapsis limb dataset observed on the dayside with SZA ≤ 75° and with the condition that at least 6 data points have been recorded within an altitude range of 115-155 km. Additionally, only limb profiles are considered that show an intensity larger than 0.1 kR in both emissions in the peak altitude region. The plot is divided into three different latitude ranges, each covering 60°, for which the maximum intensity of each 130.4 nm limb scan is plotted versus the orbit number. The upper x-axis gives the Martian season in solar longitude L_S and the MY. The color code indicates the local time (LT) of the respective scan, binned in 2 hours intervals during daytime and 6 hours intervals for nighttime. Nighttime observations have SZAs below 75° only close to the respective summer pole. Note that not all individual data points are visible due to overlapping.

The brightness varies significantly throughout the observational period, especially in the first phase of the mission when observed intensities were higher on average than later. The observed variations depend on the season, solar flux, SZA and latitude. We attempt to remove these dependencies in first order in the next paragraph by limiting the SZA range and normalizing the brightness by the solar flux. We will furthermore show the dependence on the SZA for different latitude intervals. The brightness distribution at 135.6 nm looks similar to that of Figure 2 (see supplementary material, Figure S1).

The peak altitude of the individual scans at 130.4 nm is shown in Figure 3(a). The data are displayed as a histogram due to the altitude resolution of 5 km, which would make it difficult to observe trends in a simple scatter plot. The data is binned into a grid of 5 km altitude versus 100 orbits per pixel. It should be noted that in this figure, all local times and latitudes are included. Nevertheless, a clear variation of the peak altitude with time is seen with altitude minima around Mars apoapsis and maxima around periapsis. The majority of the peak intensity altitudes fall into the range between 115-150 km. The altitude variation at 135.6 nm (Figure 3(b)) is very similar, but the 135.6 nm peak emission altitude appears more confined in its distribution.

3 Data analysis

3.1 Normalization by solar flux

Interpretation of previous Martian airglow observations had to rely on solar measurements made close to Earth that required taking into account the relative positions of Mars, Earth and the Sun, the distance of Mars to the Sun and the solar rotation. These factors naturally introduce a varying and possibly large uncertainty. Hence, direct dependences on proxies such as the F10.7 index or using the solar 130.4 nm flux observed from Earth orbit for modeling of the 130.4 nm oxygen line in the Martian atmosphere were possible only to some extent. With the availability of the EUVM instrument in Mars orbit, providing solar flux measurements and extrapolated solar, these uncertainties reduce to instrument calibration uncertainties. In the following, we investigate the direct dependence of the 130.4 and 135.6 nm lines on the solar flux by normalizing the brightness of both emissions by their respective solar forcing.

The brightness at 135.6 nm are normalized by the measured EUV flux in the following way: the energy per spectral bin given by the EUVM data is converted to the total number of photons that is able to produce photoelectrons and to furthermore excite the upper state of the $O(^5S)$ emission. This includes all wavelengths between 10 nm and 55 nm, which corresponds approximately to the ionization energy of CO_2 (13.7 eV) and O (13.6 eV), plus the energy needed to leave the oxygen atom in the $O(^5S)$ excited state of 9.14 eV (=135.6 nm). The EUV flux below 10 nm has been excluded, as these photons deposit their energy deep in the atmosphere and hence do not have a significant effect on the peak intensities. The 135.6 nm brightness is divided by the resulting number of photons. Additionally, the number of photons in the solar 130.4 nm triplet is calculated from the EUVM measurements. The brightness at 130.4 nm is divided by a weighted combination of the EUV photons (15%) and the solar 130.4 nm photons (85%). The amount of the contribution from each part comes from the model results that are discussed in Section 5.

Figure 4(a) shows the maximum brightness of each profile versus the orbit number for all data with SZA < 40°. Blue corresponds to the brightness at 130.4 nm and red to the brightness at 135.6 nm. In Figure 4(b), the brightness is normalized by the solar flux as described above and Figure 4(c) shows the solar 130.4 nm triplet flux in blue, the integrated EUV flux up to 55 nm in red and the distance from Mars to the Sun in black. EUVM observations are continuous, but only data that corresponds to the full IUVS dataset discussed here is plotted.

The observational period covers almost the complete descending phase of solar cycle 24, as can be seen in the downward trend of the solar flux intensity. This trend is overlaid by the yearly variation due to the changing Mars-Sun distance and, on a smaller scale, the solar rotation. It should be noted that the ratio between the EUV flux shown in the figure and the solar 130.4 nm line flux is not a constant, as the solar spectrum is more variable throughout the solar cycle at shorter wavelength and more constant towards longer wavelengths (Woods et al., 2015).

The normalization by the solar flux removes some of the variation, for example the highest observed intensities at the beginning of the mission are rather average after normalization. Nevertheless, the resulting intensity distribution is far from being constant and is still surprisingly complex. Strickland et al. (1973) already noted that they could not see a direct correlation between the F10.7 solar activity index and their derived oxygen intensity. Obviously, the atmosphere itself changes significantly with time. Correlation of the brightness at 135.6 nm with the EUV flux shows that 79% of the variation in the brightness can be explained by variation in the solar flux. At 130.4 nm, taking into account 15% of the EUV flux and 85% of the solar 130.4 nm flux, it is 73%. Also interesting is the intensity increase around orbit 5000. It is (i) stronger at 130.4 nm than at 135.6 nm and (ii) even more pronounced after the division by the solar flux. This feature is not related to an SZA dependence or observational bias towards the SZA and coincides with the ending phase of the dust storm period. The approximate same period one MY before, however, does not seem to reproduce this behavior.

3.2 Correlation of peak intensities and altitudes of 130.4 and 135.6 nm lines

As discussed, the excitation of the $O(^3S)$ and $O(^5S)$ excited states of oxygen are, apart from solar forcing, mainly dependent on the oxygen content in the atmosphere and to some extend on CO_2. Hence, a correlation between the intensities of the two corresponding emissions at 130.4 and 135.6 nm can be expected. Figure 5(a) shows the maximum brightness at 135.6 nm versus the brightness at 130.4 nm. A clear correlation is visible, which appears even more confined in Figure 5(b), where the brightness is normalized by the solar flux in the way described above. The corresponding correlation coefficients are 0.8 for the original and 0.75 for the flux-normalized distribution, while the reduced χ^2 for a linear fit are 112.7 and 5.5, respectively. The slope of the linear regression curve in panel (a) indicates that the brightness at 130.4 nm is on average more than twice as large as brightness at 135.6 nm.

When binning the data into 90° L_S intervals, this ratio ranges from 0.3 to 0.47 with correlation coefficients between 0.7 and 0.85 (compare Figure S2). The ratio trend follows well the changes in the solar flux at EUV wavelengths below 55 nm and the solar oxygen 130.4 nm line. There is no clear dependence on any other parameter like the solar longitude or latitude. A trend with respect to the SZA can be seen in the sense that lower intensity values of both lines are related to higher SZA, as it is expected and shown later.

The yellow triangles and blue filled circles represent the datasets that will be discussed in Section 3.4. The triangles are part of the population that is spread-out above the regression curve in Figure 5(a) and move almost exactly onto the curve after flux normalization (Figure 5(b)). During the time of observation of this specific dataset (L_S = 350, MY 32), the solar EUV flux was larger compared to the solar 130.4 nm flux than for the blue dataset (L_S = 350, MY 33). Hence, the 135.6 nm brightness is enhanced in the MY 32 dataset compared to the later one.

Figure 5(c) shows the peak brightness altitude of the two oxygen emissions plotted versus each other in a 5 km binning. The solar flux has no direct influence on the altitude of the peak emission. The peak altitudes at 135.6 nm and at 130.4 nm coincide almost perfectly, the 135.6 nm limb profiles peak appears on average slightly (but less than 5 km) lower than the ones at 130.4 nm. The brightness peaks at about 120 to 125 km. The peak altitude variation at 130.4 nm is larger than the variation at 135.6 nm. No clear correlation is observed between the intensity (non- as well as flux-normalized) and the altitude.

3.3 Dependence of the peak brightness on the SZA

Figure 6 shows the dependence of the solar flux normalized peak brightness at 130.4 nm with respect to SZA for three Martian years, MY 32 (blue), MY 33 (black) and MY 34 (green). The panels of the figure show in each row latitude intervals of 30° each, going from

North to South, and in each column L_S intervals of 90°. The plotted data do not distinguish specifically between local times. For a Chapman-like layer like the 135.6 nm emission, a dependence proportional to cos(SZA) is expected, since the photoelectron production decreases linearly with decreasing solar flux. Also, at 130.4 nm a decrease of the brightness with SZA is expected, as because of the optical thickness solar photons can be scattered before reaching large SZA due to the slant atomic oxygen density. Any deviation from this in the flux-normalized data is then due to atmospheric changes.

Towards higher latitudes, the drop in intensity with SZA is strongly pronounced. The trend is still visible at lower latitudes, but the distributions are not as confined. This might be an observational bias, as there are more data points within the low latitude datasets. In the following we briefly compare the data taken during the same Martian season but in different Martian years.

L_S 180°-270°, Northern hemisphere autumn equinox to Northern hemisphere winter solstice: This period includes perihelion at $L_S = 251°$ and usually marks the beginning of the dust storm season. There are very few data points for MY 32, but they coincide well with the data from MY 33 in the Northern hemisphere, as well as the MY 33 data coincides well with the data from MY 34 in the Southern hemisphere. In MY 33 at Southern latitudes (30°-60°) two populations are visible that correspond to different local time. The fewer data points with lower intensity that cover a larger SZA range were recorded in the morning, while the other data were taken in the afternoon. This hints to a morning-afternoon asymmetry that was observed by Stewart et al. (1992) in Mariner 9 nadir observations and will be investigated in more detail in a follow-up study.

L_S 270°-360°, Northern winter solstice to Northern Spring equinox: The flux-normalized peak brightness in MY 32 is strongly enhanced compared to their counterparts in MY 33 at equatorial latitudes and SZA around 60°. At the moment, we cannot explain this feature, but it is likely not a true SZA dependence, but rather a localized seasonal effect. This feature is much more pronounced in the non flux-normalized data and corresponds to the Southern summer in MY 32 in the Southern hemisphere close to the equator. While for MY 32 the explicit data coverage for this L_S interval is from 310° to 350° – and therefore coinciding with observed dust in the atmosphere (Montabone et al., 2015) – the data from MY 33 has been recorded between 340° and 360° solar longitude and does therefore not capture the peak of the dust season, but only parts of its end. Hence, it is likely that this enhancement around SZA = 60° is caused by dust in the atmosphere. It requires, however, further analysis.

L_S 0°-90°, Northern spring equinox to Northern summer solstice: Again, the earlier dataset (now MY 33) shows higher brightness compared to the following year (MY 34), even though the enhancement is not as strong as for the precedent datasets. Also the increased feature at SZA = 60° is still visible. Intensities within this period are on average slightly higher than in other epochs.

L_S 90°-180°, Northern summer solstice to Northern autumn equinox: For MY 33 mainly the Northern hemisphere is covered by the observations, while for MY 34 more observations have been done in the Southern hemisphere. In the overlapping region close to the equator in the Northern hemisphere, the intensities overlap well, even though the MY 34 brightness are slightly lower.

Note that caution has to be taken when drawing conclusions from this comparison. The L_S interval separation might be the same, but the observational coverage within every L_S interval is different for different MYs, as has been partly discussed above.

The behavior of the brightness of the two oxygen lines is very similar, but the dependence on the SZA seems to be less pronounced at 135.6 nm (Figures S3, S4, and S5). Additionally, in certain time periods differences are visible: L_S 0°-90° in MY 33: in Southern latitudes, the 130.4 nm intensity decreases strictly and confined with increasing SZA. For the 135.6 nm line this behavior can be seen as well, but the scatter is much larger. The same is true for L_S 270°-360°, MY 33, where the 130.4 nm brightness shows a strongly confined decrease at high SZAs at the Southern pole region. In contrast, at the same Southern latitude interval, the situation is reversed for the two lines in dataset 180°-270°, MY 33, just before the observations of the previously described dataset. Here, the brightness at 130.4 nm shows a widespread and almost constant behavior towards high SZAs, while the 135.6 nm line follows the expected trends.

3.4 Mean profiles

The individual limb profiles are quite variable and clearly represent a snapshot of the atmospheric conditions at the time of the observation. In order to provide a more qualitative analysis of the data and to investigate how the atmosphere changes with varying observational parameters, we create mean profiles from several individual limb profiles. A narrow range of observational parameters (L_S, SZA, latitude) is selected and all limb profiles corresponding to these conditions are bundled. In the following, we present two example datasets falling into the end of MY 32 (triangles, Figure 5) and MY 33 (filled circles), both at $L_S = 350°$ and in the Southern hemisphere at about -16° latitude. They each contain scans with similar SZAs, but cover different local times: in MY 32 the morning is observed while in MY 33 the early afternoon is captured. Table 1 gives the overview of the parameters of the two samples. The samples reflect interesting Southern summer conditions, just in the declining phase of the dust storms of the respective year. They have been chosen, as they are one of the few ‘observational condition sets’ that could be found to be very similar for two different MYs. Even though MAVEN/IUVS provides an unprecedented quasi-continuous dataset, and keeps filling in gaps in L_S, latitude and SZA, the combination of these three parameters is naturally complex and the same conditions have rarely been caught yet twice throughout the mission.

Figure 7 shows the sets of limb profiles for the two MYs, blue lines representing 130.4 nm limb profiles, while 135.6 nm limb scans are plotted in red. Top panels refer to MY 32, bottom panels to MY 33. The mean of all brightness profiles and the corresponding standard deviation are calculated in every 5 km altitude bin and shown by the black dots and ±1-σ horizontal bars. Again, the topside scale heights of the two emissions are notably different and conspicuously larger for the optically thick 130.4 nm triplet (199 km for MY 32 and 258 km for MY 33) and small for the optically thin 135.6 nm doublet (24 km for both datasets). The vertical profiles of both lines change significantly from one year to the other, in peak brightness as well as in peak altitude. However, within each dataset the profiles clearly represent a homogeneous group allowing the creation of meaningful average profiles, which will be compared to the corresponding modeling results in Section 5. In order to obtain the peak brightness and altitude with a resolution of 1 km, we fit the vertical profile with a polynomial near the peak altitude following Gkouvelis et al. (2018). The fit results are also listed in Table 1.

The 130.4 nm brightness dropped by 30% from MY 32 to MY 33 for the given conditions, while the 135.6 nm brightness decreased by about 45%. As for the peak altitude, the 130.4 nm emission in MY 33 deviates to higher altitudes compared to the previous year, while it remains almost unchanged at 135.6 nm.

4 Model description

4.1 Model inputs

4.1.1 Model atmospheres

We use the Mars Climate Database (MCD) Version 5.3 (Millour et al., 2009, 2017) which is based on the LMD model (Forget et al., 1999; Gonzalez-Galindo et al., 2009, 2015) to extract model atmospheres providing the respective altitude distribution of the main neutral constituents, depending on season, local time, latitude and solar activity. At the time of writing, the MCD covers climate conditions for the individual MYs 24–33 accounting for the respective EUV and dust scenarios. The dust scenario properties are based on measurements and modeling (Montabone et al., 2015).

Figure 8 shows the density profiles for the atmospheric species related to the oxygen photochemistry (CO_2, O, CO and O_2) that were extracted from the MCD. The solid lines refer to the conditions of the previously introduced dataset for MY 32 at $L_S = 350°$ and the dashed lines to one MY later (second dataset). It is clearly visible that density and temperature profiles, and therefore the density profile scale heights, have decreased as a result of the declining solar cycle.

4.1.2 Solar flux from EUVM

We generate average solar flux EUV spectra from the daily averaged data provided on the NASA PDS. Only dates that correspond to the selected limb profiles are used as input for the models. The solar 130.4 nm line intensity serving as one of the inputs for the radiative transfer code is produced following the same averaging procedure. Since the EUVM data are provided in 1 nm intervals, only a fraction of the solar flux in the interval from 129.5 nm to 131.5 nm corresponds to the 130.4 nm multiplet. This fraction is calculated to 0.77 of the full interval, after an estimate based on the high-resolution solar spectrum by the SOHO-SUMER instrument (Curdt et al., 2001). We have no knowledge how this fraction might change with time and assume it therefore to be constant.

4.1.3 Excitation and absorption cross sections

Compared to previous studies, some cross sections for the reactions of photoelectrons with atmospheric constituents have been updated. We discuss here briefly which cross sections are used for the calculations.

e + O The cross sections for electron impact on oxygen are derived from the analytical formula and parameters given in Green and Stolarski (1972) and Jackman et al. (1977) using the GLOW code (https://www2.hao.ucar.edu/modeling/glow/code). For the 130.4 nm triplet, the maximum of the cross section is 17.2×10^{-18} cm^2 at an electron energy of 20 eV and in good agreement (within ±10%) with the values from Zipf and Erdman (1985) and Johnson et al. (2003). For the 135.6 nm doublet, we scale the cross section by a factor of 0.78 in order to make it comparable to values from Zipf and Erdman (1985). The maximum cross section at 16 eV results then in 8.9×10^{-18} cm^2.

e + CO_2 For the electron impact on CO_2 resulting in 130.4 nm emission, the cross section from Mumma et al. (1972) is adapted with a scaling factor of 0.61 as suggested by Itikawa (2002), resulting in a maximum value of 6.1×10^{-19} cm^2 at 115 eV. This value is then in very good agreement with the latest measurements by Ajello et al. (2019), that provide new results at 30 eV and at 100 eV, even though the value at 30 eV is about 30% higher in the Ajello measurement than in the scaled Mumma cross section. The shape of the cross section at 135.6 nm has been measured by Ajello (1971b) and is now rescaled by a factor of 0.18, taking into account the measurements by Ajello et al. (2019). The electron impact excitation cross section reaches a maximum value of 1.9×10^{-19} cm^2 at 115 eV.

e + CO Electron impact on CO resulting in the $O(^3S)$ and $O(^5S)$ exited states is neglected in the current study as cross sections (Ajello, 1971a) and CO densities are small.
The peak cross section for the 130.4 nm triplet at 110 eV amounts to 8.0×10^{-19} cm^2 and the cross section for the 135.6 nm doublet is estimated to be smaller by a factor of 0.85 (6.8×10^{-19} cm^2 at 100 eV). According to Ajello et al. (2019) the cross section for the $O(^3S)$ production (130.4 nm) is slightly higher (8.8×10^{-19} cm^2 at 100 eV), but even significantly

lower for the O(^{5}S) state (135.6 nm): 1.8 × 10^{-19} cm^2 at 100 eV. The values are therefore comparable with the cross sections for electron impact on CO_2, but at the respective altitudes between 100 and 150 km, the CO density is at least an order of magnitude smaller than the CO_2 density. Also, the contribution by electron impact on CO_2 is already a minor source for both oxygen lines, so that the CO-impact source can safely be ignored.

e + O_2 The cross section for electron impact on O_2 is 11.4 times less than the one for electron impact on oxygen for the 130.4 nm line (Stone and Zipf, 1974). The cross section for the 135.6 nm emission is not known, but is most likely even smaller. Furthermore, the O_2 density is about two orders of magnitude lower than the CO_2 density; hence, we neglect this process here for both emissions.

Absorption by CO_2 During the modeling process, absorption processes due to CO_2 must be considered. Firstly, the solar flux is accordingly attenuated as it penetrates the Martian atmosphere and secondly, when integrating the emissions from the O(^{3}S) and O(^{5}S) excited states, the CO_2 content along the line of sight is taken into account. The CO_2 absorption cross section is rather large at EUV wavelengths below 100 nm that produce the photoelectrons (in the order of a few 10^{-17} cm^2, Huebner et al., 1992) and the solar flux at these wavelengths is normally fully absorbed at altitudes below 70 km. On the other hand, the CO_2 absorption cross section values at 130.4 and 135.6 nm are small. Still, they contribute significantly to the characteristics of the observed limb profile (Section 5.1). At these wavelengths, the high resolution cross sections from Venot et al. (2018) at 150 K are being used: 1.14 × 10^{-18} cm^2 (130.22 nm), 6.77 × 10^{-19} cm^2 (130.49 nm), 5.93 × 10^{-19} cm^2 (130.60 nm), 5.3 × 10^{-19} cm^2 (135.56 nm), 8.85 × 10^{-19} cm^2 (135.85 nm). For a cross section of 1 × 10^{-18} cm^2 the vertical optical depth for absorption by CO_2 becomes unity at 105 km.

4.2 Models

4.2.1 Monte Carlo code

Monte Carlo simulation for the calculation of the photoelectron production by the solar EUV flux penetrating the model atmosphere are used in this study. The resulting photoelectron spectrum is a function of altitude between 400 and 60 km above the surface with a spatial resolution of 2 km between 60 and 190 km and 5 km between 190 and 400 km. Calculations of the collisional sources are based on the Direct Simulation Monte Carlo

(DSMC) method that has been developed to calculate the brightness profiles of emissions of the Earth, Jupiter, Saturn, Venus and Mars atmospheres (Shematovich et al. 2008; Gérard et al., 2008). Collisional excitation rates including photoelectron impact and photodissociation in combination with the respective atmospheric densities are calculated. Finally, the total volume production rates are obtained as a function of altitude, which is integrated along the line of sight to simulate limb observations in the optically thin case.

4.2.2 Radiative transfer code

For the 130.4 nm triplet we combine the photoelectron volume excitation rates of the O(^{3}S) state from the Monte Carlo code with calculations for the production rate from the solar 130.4 nm line. The line shape of the solar triplet is taken from Gladstone (1992) and is normalized using on the reconstructed solar spectra based on the EUVM measurements as described before. For these two sources we employ the REDISTER radiative transfer code from Gladstone (1985) and calculate the effects of multiple scattering including angle-averaged partial frequency redistribution. This allows photons to escape an optically thick atmosphere by scattering in frequency from the core of the line into the optically thin line wings. The cascading contribution from upper levels is taken into account by using the 'optically thick' cross sections from Zipf and Erdman (1985). The population of the ground state sublevels is assumed to be proportional to the degeneracy of the sublevels, i.e. to 2J+1, with J = 2, 1 and 0 for 130.2, 130.5 and 130.6 nm, respectively. This is equivalent to a thermal distribution as shown by Hubert et al. (2015) for the Earth. Furthermore Rayleigh scattering is included with its cross section is derived from the polarizability of the CO_2 molecule. Instead of using g-factors in the calculations, the scattering of the solar radiation is explicitly taken into account by the radiative transfer code, thus giving internally the primary source of photons due to scattering of the solar flux. The modeling methodology that we use is indeed similar to the one followed by Hubert et al. (2010) for the upper atmosphere of planet Venus, except that we can take advantage of the direct measurement of the solar EUV flux. The resulting optically thick source function, again, is integrated along the line of sight applying the formal solution of radiative transfer in order to obtain limb profiles. The atmosphere becomes optically thick ($\tau > 1$) at the respective line centers (130.2, 130.5 and 130.6 nm) below approximately 270, 255 and 215 km (MY 32) and below 240, 225 and 195 km (MY 33). At 130 km altitude it reaches an optical depth of τ = 89, 53 and 18 for the atmosphere of MY 32. The corresponding values for MY 33 are τ = 52, 31 and 10.

5 Modeling the observations

In order to better understand how the two oxygen emissions respond to changes in the atmospheric density profiles, the temperature profiles and the solar flux, we perform sensitivity tests. It is understood that the density profiles of the atmospheric constituents and the temperature profile are strongly linked and not independent of each other. Hence, the results of the sensitivity tests should not be interpreted in absolute values, but rather tendencies in the behavior of the observed peak brightness and altitude of the two oxygen multiplets can be derived.

5.1 Sensitivity to atmospheric constituents

For the sensitivity tests, the atmosphere of MY 32 (Figure 8, solid lines) is used and oxygen and CO_2 densities are scaled individually, while the densities of all other atmospheric constituents are being kept. These two species are considered to be the dominant contributors to emission and/or absorption of the two lines. Additionally, all atmospheric constituents are scaled with the same factor. The changes in the peak brightness and its altitude are investigated. Figure 9 shows the results. Top panels display the respective peak brightness in kR as a function of the atmospheric scaling factor, while bottom panels show the corresponding dependence of the peak brightness altitude. The red solid line represents the total brightness at 135.6 nm, which is the sum of the electron-impact contribution on O and CO_2. The blue dashed-dotted line is the contribution of electron impact on O and CO_2 to the 130.4 nm brightness and the dashed line the contribution resulting from the resonance scattering of the solar 130.4 nm flux and subsequent radiative transfer. The solid blue line shows the sum of both contributions. For comparison, the peak brightness and peak brightness altitude of the corresponding mean profile (Figure 7(a,b), Table 1) is added to the plots as data points at scaling factor unity. Note that the ‘steps’ in the altitude dependence of the emission is due to the spatial resolution of the model atmosphere, which is approximately 2 km at these altitudes.

Oxygen density (Figure 9**(a,f)):** As expected for an optically thin emission, the brightness at 135.6 nm rises almost linearly with increasing oxygen content. At 130.4 nm, this dependence is much less linear, but it is not as flat as expected for an optically thick emission. This is contrary to the assumption that the 130.4 nm triplet brightness is rather insensitive to the oxygen abundance (e.g. Strickland et al, 1973). The extended optically thin wings of the line triplet are likely to contribute significantly to the brightness at the peak, as has been suggested by Gladstone (1988) for the Earth and by Chaufray et al. (2015) for Mars. At higher altitudes, where the contribution of the optically thick line core is more dominant compared to the wings, the brightness increase with O density increase should be smaller. Notable is also that with increasing oxygen density the photoelectron-impact contribution becomes more important compared to resonance scattering. For the shown example atmosphere, the contribution rises from 18% for no scaling to 33% for a scaling factor of 4. Our understanding is that the solar contribution remains largely determined by the solar flux and is therefore less sensitive to the oxygen density, while the electron-impact excitation rate is proportional to the number of electron-oxygen collisions that occur per second. Hence, increasing the oxygen density increases the primary input of emitted photons into the system, resulting in a near linear dependence.

The altitude dependence of both lines is rather flat indicating that the oxygen abundance has almost no influence on the observed peak altitude. This can be also seen implicitly in the 130.4 nm study by Chaufray et al. (2015, Figure 3). Again, the extended optically thin line wings at 130.4 nm could explain the extremely weak dependence on the peak brightness altitude. The slight decrease in altitude at 130.4 nm is most likely owed by the changing importance of the two contributions (resonance scattering and electron impact) whose primary source functions peak at slightly different altitudes, and also by the different scale height of these source functions. This is then smeared out by the radiative transfer, which allows the observer only to penetrate the atmosphere to distances that correspond approximately to where the optical depth becomes unity. These results show also the difficulty and complexity of interpreting optically thick emissions, especially so close to the homopause of the atmosphere.

CO_2 density (Figure 9**(b,g)):** With increasing CO_2 density, the peak brightness of both oxygen emissions decreases. This is (i) due to absorption of the penetrating solar light at EUV and 130.4 nm wavelengths, which results in lower production rates and (ii) because of the absorption at 130.4 and 135.6 nm along the line of sight of the observer.

This effect also strongly influences the observed altitude of the peak intensity that increases significantly with increasing CO_2 density, since photons produced deep inside of the atmosphere are unable to reach any instrument located at high altitude. The solar flux cannot penetrate as deep into the atmosphere, so that the photoelectrons are produced at higher altitude. The emission is additionally cut on the lower end by the absorption of the denser CO_2 atmosphere below. Hence, the altitude of the observed brightness peak can be used as an indicator for the CO_2 density rather than the oxygen density. The observed range of peak altitudes (Figure 3) indicates that the CO_2 density changes by factors larger than 5 within a MY.

All atmospheric constituents (Figure 9**(c,h)):** At first glance the combined effects of the changes in the oxygen and CO_2 density appear as a superposition of the effects to the peak intensity and altitude as described before. The brightness increases with increasing atmosphere density, but the attenuation by CO_2 diminishes the magnitude. The altitude behaves like for the CO_2 scaling, as the oxygen density has almost no influence. Caution should be taken when interpreting these results though, as the simple scaling of the atmospheric constituents leads to different changes in the atmosphere, due to the different scale height of O and CO_2: both species do not experience the same temperature profile with the same scaling factor. Tests with isothermal temperature profiles show, however, that this effect is not very strong.

5.2 Dependence on the temperature profile

The temperature profile of the atmosphere defines the scale height of the vertical O and CO_2 density profiles. It is assumed to be isothermal in the exosphere (above ~200 km) and influences the Doppler width in the radiative transfer model that grows with increasing temperature. Chaufray et al. (2009) found an increase in brightness at 130.4 nm with increasing exospheric temperature at high altitudes (above 250 km) and at the same time a decrease at lower altitudes. The temperature profiles below the exobase are rather complex and rapidly changing in the region of the observed peak emission (Figure 8(b)). In order to simplify, we apply isothermal temperature profiles between 150 and 350 K for the sensitivity study. This means running the simulations without changing the density profiles of the atmospheric components, but only modifying the temperature profile to a constant profile of one temperature at a time. This is obviously not 'physical' and a change of the temperature profile influences the scale height of the atmospheric constituents (see also discussion on scale height in Section 5.4), but this approach shall only demonstrate general dependencies. The results are shown in Figure 9(d). As reported by Chaufray et al. (2009), the peak brightness at 130.4 nm decreases slightly with increasing temperature, but not at 135.6 nm. The peak brightness altitude, however, does not show any change within the tested parameter range and is therefore not displayed. The changes in brightness can be almost neglected compared to the effects of changing atmospheric constituents and also compared to the changes induced by the solar flux variability.

5.3 Dependence on the solar flux

The solar flux at Mars varies over the course of the collected dataset by ±60% for the EUV and a bit less for the solar 130.4 nm line due to the solar cycle and the varying Sun-Mars distance. The dependence of both lines on the solar flux is strictly linear as seen in Figure 9(e). The solar flux here is scaled the same for all wavelengths even though we know that the changes in the solar spectrum are wavelength-dependent to some extent. For the example atmosphere, the variations in the solar flux can infer brightness changes as large as ±0.4 kR at 135.6 nm and ±0.65 kR at 130.4 nm. This order of magnitude roughly covers the brightness changes observed during the mission up to now. Note, however, that this is without taking into account the effect of the SZA meaning that the changes in the solar flux cannot fully explain the changes in the observed oxygen dayglow brightness. As seen before, it explains about 70-80% of the changes. The resulting variations then, indeed, reflect changes in the atmospheric structure and composition.

The solar energy injected into the Martian atmosphere modulates the atmospheric structure (Bougher et al., 2017), but other than that it has no direct influence on the altitude of the observed peak, at least within a reasonable range of variation. A significant modification of the balance between electron-impact sources and the resonance scattering of the solar line source of photons could lead to a modification of the peak altitude at 130.4 nm. This, however, would be more likely to happen if the flux scaling were made wavelength-dependent.

5.4 Modeling individual cases

The results of modeling the two datasets shown in Figure 7 are displayed in Figure 10. Panel (a) shows the results for the dataset taken in MY 32 and panel (b) for the dataset taken in MY 33. As before, results at 130.4 nm are shown in blue and at 135.6 nm in red. The data is given as filled circles with the 1-σ variation of the respective dataset as horizontal bars. The model result of the total brightness is represented by the solid lines, which is the sum of a main contribution (dashed line) and a minor contribution (dashed-dotted line). At 130.4 nm, the major contribution arises from resonance scattering of the 130.4 nm solar flux and the minor contribution results from electron impact on O and CO_2. Electron impact on oxygen is by far the dominant source at 135.6 nm with only very little contribution of electron impact on CO_2. The modeled and observed peak brightness and altitude results of the model are given in Table 1.

Peak brightness: At the peak altitude of the model simulations, the contribution of solar flux to the 130.4 nm triplet brightness is 80% for the first dataset (a) and the remaining 20% result from photoelectron impact. For the second dataset (b), this ratio is 84% to 16%. The latter ratio has been used for the flux normalization that was discussed earlier. For the peak brightness of the 135.6 nm doublet, electron impact on O contributes 96% for MY 32 and 94% for MY 33 of the total emission for both datasets, making the contribution of electron impact on CO_2 rather negligible. Except for the 130.4 nm brightness in MY 33 (+4%), the model results seem to slightly underestimate (-5%) the observed brightness. However, given the excitation cross section uncertainties and the combined uncertainty of the absolute calibration of the IUVS detector and the EUVM instrument as well as in the model atmospheres, these results are in excellent agreement and well within the variability of the dataset.

Comparing the two datasets, the brightness at 130.4 nm decreases by 30% from MY 32 to MY 33 for the given dataset, while at 135.6 nm it drops by about 45%. The ratio of the peak brightness of the two oxygen lines changes from 0.59 to 0.46. The model atmospheres show a 34% decrease in the CO_2 density and a 43% decrease in the atomic oxygen density at 130 km, which is in good agreement with the calculated intensity changes. Regarding the solar input, the average solar flux between 0–55 nm drops by 39% and the flux in the solar 130.4 nm line by 6% with respect to the MY before.

Peak altitude: For the definition of the altitude grid, IUVS uses the IAU reference ellipsoid with equatorial radius = 3396.19 km and average polar radius = 3376.20 km (NASA PDS) and the MCD was run with a reference radius of 3396 km. The altitudes were then converted to the IAU ellipsoid. For the MY 32 dataset, the observed limb peak altitude at 130.4 nm is extremely well reproduced by the model within the uncertainties. The offset is larger for the dataset of MY 33, in which the fitted observed limb profile reaches its maximum about 5 km above the model maximum. The brightness at 135.6 nm peaks in the IUVS observations about 3 km below the model for the first and 3 km above the model for the second dataset. The vertical resolution of the MCD at these altitudes is 2 km.

In contrast to the peak brightness, the observed peak altitude is not dependent on the absolute calibration of IUVS and EUVM. It depends on the atmospheric densities and the CO_2 absorption cross sections. The cross sections are the same for both model runs. As the optically thin emission at 135.6 nm is easier to interpret, we rely on the oxygen doublet results for a tentative scaling of the atmospheric components in order to match the model to the observations. Note that for this scaling and the derived results, we do not modify the temperature profile of the MCD atmospheres, which would be beyond the scope of this study. The atmospheric densities of the MCD are scaled by a factor of 0.7 in order to match the altitude, and the oxygen density is afterwards increased by a factor of 1.1 in order to match the intensity. These changes lead to a good agreement of the 130.4 nm brightness as well, while the model limb profile will peak 2 km below the IUVS observations. In order to match the peak altitudes for MY 33, an increase in the atmospheric density by 1.5 would be required, with a subsequent increase of the oxygen density by 20%. This will, however, overestimate the brightness at 130.4 to outside the variability of the dataset.

Scale height: The observed 135.6 nm intensity nicely follows a Chapman layer and its topside scale height is well reproduced by the model especially for the first dataset. The scale heights of the IUVS observations are about 24 km and of the model results 23 km for MY 32 and 20 km for MY 33. Contrarily, at 130.4 nm, a change in the scale height can be seen at altitudes between 160 and 180 km, where the model scale height deviates from the observed mean profile. The model therefore underestimates the observed scale height significantly with about 155 km in the model to 199 km in the observations in MY 32 and 133 km to 256 km in MY 33. During the study, this change in scale height has been observed in many of the produced mean profiles. The model is not able to reproduce this characteristic, as it includes no process that would cause this feature. Reasons for this scale height change may include a hot oxygen population, which is currently not considered in the model and is also not expected at these altitudes, but has been observed at much higher altitudes (~500 km, Deighan et al., 2015). The corresponding simulated brightness excess has been calculated to be in the order of only 10 to 20 R (e.g. Lee et al., 2015; Leblanc et al., 2017). Also Chaufray et al. (2016) conclude that the effect of a hot oxygen component should not change the dayside emission rate of the thermal oxygen component. Another possibility is a mismatch in the shape of the temperature profile in the atmospheric model as resonance scattering cross section is inversely proportional to the temperature (T) by $T^{-0.5}$ and therefore sensitive to thermal profile in the atmosphere. The exospheric temperature derived from NGIMS measurements during the second Deep Dip campaign (April 2015, L_S = 329°, Bougher et al., 2015) are in the order of 275 K, while the MCD calculates for the same conditions significantly lower temperatures of around 200 K. As the NGIMS measurements are close in time and similar to the observing conditions to the first period studied here, we can assume the temperature profile provided by the MCD for our study is not accurate. Another factor could be a mismatch in the oxygen density profile of the MCD. It also should be noted that the illumination conditions at the spacecraft position and at the tangent point may be different and since the atmosphere is optically thick at 130.4 nm, the observed profile does not necessarily coincide completely with the conditions at the tangent point. Also, the fact that the scale height difference is more pronounced in the dataset with a weaker brightness could indicate a diffuse background emission with a large scale height. Interestingly, the bottom side scale height nicely agrees at 130.4 nm, while the model is not able to reproduce it at 135.6 nm. A reason for the mismatch can be that the calculation of the photoelectron flux caused by the short wavelength part of the solar EUV radiation is inaccurate in the Monte Carlo code below the peak due to the large numerical noise at this altitude.

Oxygen mixing ratios: From the model atmosphere we derive [O]/[CO_2] mixing ratios. For the dataset from MY 32 we find a ratio of 2.9% at 130 km, which is slightly higher than previously reported mixing ratios from UV dayglow observation, but are comparable to results from photochemical equilibrium calculations (e.g. Fox and Dalgarno, 1979). When we then apply the previously discussed scaling factors (n_{CO2} × 0.7, n_O × 0.77) based on the observations at 135.6 nm, we derive a mixing ratio of 3.1%. For the MY 33 dataset, the mixing ratio is 2.5%. If a scaling factor of 1.5 is applied to the CO_2 density and a factor of 1.8 to the oxygen density, this ratio increases to 3.0%. However, it should be noted that the uncertainties in the IUVS brightness are also in this order of magnitude, as will be discussed below.

5.5 Error sources and uncertainties

Absolute calibration of UV spectrographs is a challenging task and the IUVS FUV channel intensity calibration is currently estimated to be reliable up to ±25% (Jain et al., 2015). PDS versions 7 and 13 are used. Furthermore, the extraction algorithms for the spectral line derivation removing contributions from blended lines at the respective wavelengths can play a role. The (14,3) line from the CO 4th positive bands falls into the line wing of the 130.4 nm oxygen emission and the CO 4th positive (14,4) line emission overlaps with the 135.6 nm emission. Another source of uncertainty is the absolute calibration of the EUVM instrument at EUV wavelengths and at 130.4 nm, and the model. The total uncertainty between 10 nm and 55 nm is wavelength dependent (see Figure 3(c) in Thiemann et al., 2017) and at 130.4 nm ~10%.

The excitation cross sections have been updated frequently during the last years, using measurement with more sophisticated experiment setups. While the shape of the cross sections for electron impact on O and CO_2 leading to oxygen atoms in the excited states O(^{3}S) and O(^{5}S) is thought to be well known, their absolute magnitude was changed sometimes by factors of 3 or more. Assuming the instrument calibration to be accurate, the current study could imply that the latest magnitudes of the all cross sections are now rather well constrained. Nevertheless, studies and discussions are ongoing. For example the recent analytical study of the cross section by Tayal and Zatsarinny (2016) suggests the optical emission cross section for electron impact on O leading to the emission at 130.4 nm is smaller by a factor of 0.6 at the peak electron energy (20 eV) and different in shape, thereby being lower than most cross section measured or calculated until then. This case would affect the calculated brightness from this process accordingly, but by less than a factor of 0.6, as the shape of the cross section is flatter and almost converging with previous published results towards higher electron energies (Tayal and Zatsarinny, 2016, Fig. 15).

Finally, the model atmosphere densities have their uncertainties as well. From our results we conclude that the uncertainty in the CO_2 density can easily be as large as a factor of 1.5. This is also indicated by results using IUVS observations of the CO_2^+ UV doublet at 298-299 nm. Another uncertainty is the temperature profile above 100 km, as discussed above (see scale height discussion). Obviously, the temperature profile influences the density profiles of all species. Regarding the altitude modeling, a small uncertainty is introduced as the covered latitude range of the datasets translates into an altitude range of ±0.6 km when converting the altitude grid of the model to the IAU reference ellipsoid.

6 Summary and discussion

We present an overview of two Martian years (MYs) of atomic oxygen dayglow limb observations in the UV at 130.4 nm and 135.6 nm. The line multiplets are emitted from the OI(^{3}S) and OI(^{5}S) excited states, respectively. This is the first time since the Mariner 6/7 observations that results for the oxygen emission at 135.6 nm are analyzed. The data has been recorded between 2014 and 2018 with the IUVS instrument on board the MAVEN spacecraft.

From the extracted peak brightness of all available limb data with an SZA lower than 75°, we observe that the highest intensities have been recorded in the beginning of the mission, owing to the higher solar activity at that time. The MAVEN mission started shortly after the maximum of solar cycle 24 and was approaching minimum conditions at the end of the dataset described here. The observed limb peak brightness varies between 0.2 and 1.8 kR at 130.4 nm and between 0.1 and 1.1 kR for the 135.6 nm emission.

Normalization of the peak brightness by in situ EUVM solar flux measurements (only solar EUV flux between 10 and 55 nm for 135.6 nm and a combination of this flux (16%) and the solar 130.4 nm flux (84%)) does not remove all the variability in the brightness. The solar flux is responsible for about 70-80% of the observed brightness variations; the remaining part arises from atmospheric changes. While the flux normalization reduces on average the variability of the observed intensities in both oxygen multiplets, for some observations it enhances the variability for the 130.4 nm triplet, but not of the 135.6 nm doublet. The time of the observations showing this behavior coincides with the end of the dust storm season at the end of MY 33 and the beginning of MY 34 and remains still to be explained.

We also find that the behavior of the two multiplets (in terms of variability of the peak brightness and the peak altitude) is very similar. The 130.4 nm line appears slightly more variable, but both follow the same general trends. Direct comparisons of the peak brightness at 135.6 nm and 130.4 nm lead to correlation coefficients of 0.78 for the non-normalized data and of 0.76 for the flux-normalized data with a reduced χ^2 for a linear fit of 112.7 and 5.5, respectively. On average, the 130.4 nm brightness is larger by a factor of 2.2 than the brightness at 135.6 nm observed at the same time. This factor varies between 2.1 and 3.4 when binning the data into 90° solar longitude intervals. It is primarily driven by the solar cycle influence and only secondarily by the season and the ratio decreases with declining solar cycle. This is because the short wavelength part of the solar spectrum changes stronger throughout the solar cycle than the longer wavelength part (Woods et al., 2015). For example the average flux below 55 nm dropped by 39% from May 2015 to April 2017 (corresponding to L_S = 350° in MY 32 and 33), while the solar intensity at 130.4 nm dropped by only 6% within the same time frame.

The dependence of the flux-normalized peak brightness on the SZA is very similar for both lines, more pronounced at 130.4 nm and stronger at higher latitudes, even thought the latter might be an observational bias. An intensity enhancement around 60° SZA for the time in the end of MY 32 and begin of MY 33 at equatorial latitudes is observed, but not yet explained. A possible candidate for changes in the atmosphere at the end of a MY is a (global) dust storm. Furthermore, hints for a morning-afternoon asymmetry are visible in the observed brightness, featuring excess in the afternoon brightness, which has been reported earlier by Stewart et al. (1992) in nadir observations of Mariner 9. This will be investigated in more detail in the future.

The observed altitudes of the peak emissions coincide well for the two emissions, the 130.4 nm limb profiles peak between 120 and 125 km, with the 135.6 nm profiles peaking on average less than 5 km lower. From individual limb profiles we find the highest observed peak brightness altitudes are 155 km during Southern summer (L_S = 270°) close to the Southern pole and the lowest observed altitudes are 105 km at equatorial regions during Northern hemisphere Summer (L_S = 90°). Note that this can be biased, as Northern and Southern hemisphere are not equally covered by the observations for the same time periods. But due to the varying distance to the Sun, the Martian atmosphere is known to expand and contract (e.g. Bougher et al., 2017) and the maximum and minimum altitudes with respect to solar longitude would be expected to behave accordingly. The solar flux intensity on the other hand has no direct influence on the altitude of the peak brightness.

Mean limb profiles have been created for a narrow range of observational parameters and two sets are presented for similar conditions in different MYs (MYs 32 and 33): SZA ≈ 34°, latitude ≈ -16°, L_S = 350°. The observed intensities vary from one year to the other (decrease from MY 32 to MY 33) by 30% at 130.4 nm and by 45% at 135.6 nm, while the altitude increases slightly from 126 to 128 km for the 135.6 nm emission and from 128 to 131 km for the 130.4 nm emission. The two datasets are modeled using model atmospheres from the MCD, solar flux measurements from EUVM, Monte Carlo calculations for electron impact on atomic oxygen and CO_2, and additionally radiative transfer calculations for multiple scattering at 130.4 nm.

The 130.4 nm triplet is mainly produced by resonance scattering of the solar 130.4 nm radiation by oxygen atoms (in the order of 80% to 85% for the modeled examples) and secondly by electron impact on O and CO_2. Electron-impact cross sections have been updated and lead to the conclusion that electron impact on oxygen is the main contributor (95%) for electron-impact induced emission at 130.4 and 135.6 nm. Only about 5% arise from electron impact on CO_2, while all other processes (electron impact on CO and O_2, and photodissociation) are negligible. The photoelectron-impact contribution at 130.4 nm grows almost linearly with oxygen density. For the shown example atmosphere, its contribution rises from 16% for no scaling to 26% when the oxygen density is scaled by a factor of 4.

The limb profiles feature different topside scale heights with respect to the two emissions. It is in the order of 20 km for the optically thin 135.6 nm emission and significantly larger (exceeding 100 km) at 130.4 nm at which the Martian atmosphere becomes optically thick below 290 and 255 km for the two selected datasets. The vertical optical depth reaches $\tau = 161$ and $\tau = 93$ at 130 km, respectively. The mean limb profiles at 130.4 nm show a change in scale height between 160 and 180 km, which is not reproduced by the model. An explanation could be a diffuse background from a hot oxygen population, but this is expected at higher altitudes (Deighan et al., 2015) and to contribute only very little to the total brightness (Lee et al., 2015; Leblanc et al., 2017). Another more likely possibility is a not well-matching vertical temperature or oxygen density profile from the MCD. This is suggested by NGIMS measurements showing profiles with significantly higher temperatures (Bougher et al., 2015). Also, effects due to the optical thickness may play a role, as the limb profile observed by the spacecraft does not necessarily coincide with the actual observational conditions (SZA, latitude) at the tangent point. This scale height change requires further investigation.

Sensitivity tests show that the CO_2 density influences to some extent the peak brightness and strongly the peak brightness altitude of the two emissions by its absorption properties. Considering the observed peak brightness altitude range of 115 to 150 km over the course of the observations, this indicates changes in the CO_2 density by more than a factor of 5. The oxygen density influences mainly the brightness of the multiplets, nearly linearly at 135.6 nm, and less linear, but surprisingly strong, for the optically thick 130.4 nm emission. This is likely due to the contribution of the extended optically thin wings of the emission. The solar flux affects the observed maximum limb brightness linearly, but not its altitude, while the temperature affects slightly the peak brightness at 130.4 nm and does not affect the peak brightness altitude under the artificial condition that the atmospheric density profiles are not changed.

From the model atmospheres we calculate $[O]/[CO_2]$ mixing ratios at 130 km for the two analyzed datasets and find 3.1% for the dataset in MY 32, which includes an atmospheric scaling factor of 0.7 for CO_2 and 0.77 for O in order to match the observations. For the dataset in MY 33, the ratio is 3.0% using scaling factors of 1.5 for the CO_2 density and 1.8 for the O densities. These values have been derived using model sensitivity tests and the results of the peak brightness and altitude at 135.6 nm. These results are in less agreement with the 130.4 nm observations, but considering the overall uncertainties still a good match. The mixing ratios are larger than previously reported values based on UV dayglow observations at 130.4 nm, which are in the order of 0.5% to 1.2% (e.g. Strickland et al., 1973; Chaufray et al., 2009), but comparable to results from early photochemical equilibrium calculations (e.g. Fox and Dalgarno, 1979; Hanson et al., 1977). They also coincide well with NGIMS measurements from Deep Dip 2, taken at L_S = 329.5° at 4° Southern latitude (Stone et al., 2018) and SZA between 5° to 10° that resulted in a mixing ratio of about 3.3% (Fox et al., 2017). As a result, the two shown examples of our study do currently not support the new photochemical equilibrium calculations from Fox et al. (2017) that show higher mixing ratios than NGIMS by a factor of 4.

It is now clear from MAVEN data that large variations in the observed peak brightness of the two oxygen emissions are a fact. With respect to solar activity, the IUVS dataset (declining phase of solar cycle 24) covers observations from Mariner 9 (declining phase of solar cycle 20) and SPICAM (declining phase of solar cycle 23), while the Mariner 6/7 observations were collected at higher solar activity (solar maximum of solar cycle 20). Those observations were taken at L_S = 200° (at the beginning of the dust season and between Northern hemisphere autumn equinox and perihelion) at SZA = 27° and 44° during MY 8 and the observed brightness were 0.8 kR at 130.4 nm and 0.4 kR at 135.6 nm (Barth et al. 1971). Given the higher solar activity that time, the emissions are lower compared to what has been observed with IUVS for similar conditions. Mariner 9 data (Strickland et al., 1973) were collected between L_S = 294° and L_S = 320° (late Southern summer, dust storm season) of MY 9 at latitude = -45° and at around 10am local time (SZA = 31° to 36°). At 130.4 nm they reported peak brightness of 0.8 kR, which, again, is lower than IUVS observations under similar conditions. The SPICAM observations at 130.4 nm shown by Leblanc et al. (2006) demonstrate the brightness rising from 0.3 kR at high SZA to 0.65 kR at low SZA during Northern hemisphere summer. While the high SZA numbers are consistent with IUVS results, at low SZA the intensity seen by SPICAM is lower by up to a factor of 2 for MY 33 but by less than this for MY 34. In summary, even though it seems that IUVS is generally observing larger brightness than its predecessors, it is not possible to conclude a systematic offset due to the strong variability on the individual limb scans. It is the first time that it is possible to investigate a large number of limb profiles of the same observational conditions, allowing to deduce general trends and dependencies of the involved parameters.

Future work will take advantage of this in order to have a more detailed look into specific conditions, as for example during the dust storm seasons, and also to derive oxygen mixing ratios in dependence of temporal and spatial variations.

7 Main conclusions

- For the first time since Mariner, the O 130.4 nm and 135.6 nm lines have been studied simultaneously. Even though the Martian atmosphere is optically thick at 130.4 nm and optically thin at 135.6 nm, the peak brightness and the peak brightness altitude of the limb profiles of both emissions are strongly correlated. This indicates a rather straight forward photochemistry, matching today's knowledge of the excitation processes of the O(^{3}S) and O(^{5}S) excited states.
- The photochemistry of the two emissions involves mainly atomic oxygen for the production (solar resonance scattering of O atoms (~20%) and electron impact on O (~80%) at 130.4, nm and electron impact on O (~95%) at 135.6 nm), with very minor contributions of electron impact on CO_2. CO_2, on the other hand, plays a major role in the attenuation of the observed profiles, by absorption of the incoming solar radiation and photoelectrons, thereby reducing the production rate, and by absorption along the line of sight of the dayglow emission.
- The changes in the peak brightness and altitude of the limb profiles at 130.4 and 135.6 nm that are observed over the course of two Martian years and the declining solar cycle cannot be fully explained by the solar flux influence itself, but rather indicates a change of more than a factor of 5 in the CO_2 density with time. The expansion of the atmosphere is strongly visible by the varying peak brightness altitude being largest during perihelion and lowest during aphelion. Also, in the solar flux-normalized brightness of the two emissions, differences between different Martian years are visible, especially during the dust storm season.
- The peak altitude is strongly dependent on the CO_2 density profile, while the intensity depends on both, O and CO_2. Therefore, the CO_2 column density at this altitude can be derived and in combination with the knowledge of the peak

brightness, it should be possible to deduce directly [O]/[CO_2] mixing ratios from the observations. This will be future work.

- The peak brightness dependence on the SZA seems more pronounced at higher latitudes, which is likely due to the cooler and therefore less variable atmospheric temperature. We also find hints to a morning-afternoon brightness asymmetry.
- The model atmospheres provided by the MCD appear to describe well the Martian atmosphere as Monte Carlo and radiative transfer modeling of the two emissions reproduce the observed limb profiles reasonably. The solar forcing in these models is extremely well confined as we use EUVM measurements at Mars as an input. We are, however, not able to exactly reproduce the scale height at 130.4 nm, which is probably caused by an inaccurate temperature profile in the MCD.
- From two test cases, we report [O]/[CO_2] mixing ratios derived from the model atmospheres that are in good agreement with the latest in situ mass spectrometer Deep Dip data from NGIMS, that appear to be slightly larger than previously reported mixing ratios from remote UV airglow observations and that are lower than the latest reported values from photochemical equilibrium calculations.

Acknowledgements and Data

B.R. acknowledges financial support by Belgian Federal Science Policy Office (BELSPO) SCOOP/BRAIN research contract. L.G. acknowledges financial support from BELSPO via the PRODEX Programme of ESA. B.H. is supported by the Belgian Fund for Scientific Research (FNRS). This research was supported by NASA through the MAVEN project._The IUVS and EUVM MAVEN datasets were obtained from NASA's Planetary Data System (PDS) available at http://atmos.nmsu.edu/data_and_services/atmospheres_data/ MAVEN/maven_main.html. The IUVS data used in this study is level 1C version 07 (for orbits 3334 to 4138) and version 13 (for all other orbits) data. This work utilized the RMACC Summit supercomputer, which is supported by the National Science Foundation (awards ACI-1532235 and ACI-1532236), the University of Colorado Boulder, and Colorado State University. The Summit supercomputer is a joint effort of the University of Colorado Boulder and Colorado State University. The

Mars Climate Database (version 5.3) is available on line at http://wwwmars.lmd.jussieu.fr/mars/access.html. We thank V. Shematovich and D. Bisikalo for helpful discussions on the Monte Carlo code. The GLOW code is available from https://www2.hao.ucar.edu/modeling/glow/code

References

Ajello, J.M., Emission Cross Sections of CO by Electron Impact in the Interval 1260 – 5000 Å. I, J. Chem. Phys. 55, 3158 (1971a); doi: 10.1063/1.1676563

Ajello, J.M., Emission Cross Sections of CO_2 by Electron Impact in the Interval 1260–4500 Å. II, J. Chem. Phys. 55, 3169 (1971b); doi: 10.1063/1.1676564

Ajello J. M., C. P. Malone, J. S. Evans, G. M. Holsclaw, A. C. Hoskins, S. K. Jain et al., UV Study of the Fourth Positive Band System of CO and OI 135.6 nm from Electron Impact on CO and CO_2, 2019, Journal of Geophysical Research – Space Physics

Barth, C. A., C. W. Hord, J. B. Pearce, K. K. Kelly, G. P. Anderson, A. I. Stewart, Mariner 6 and 7 Ultraviolet Spectrometer Experiment: Upper Atmosphere Data, 1971, Journal of Geophysical Research, Vol. 76 Nr. 10

Barth, C. A., The atmosphere of Mars, 1974, Ann. Rev. Earth Planet. Sci., 2, 333–367.

Bougher, S. W. and R. G. Roble, Comparative Terrestrial Planet Thermospheres 1. Solar Cycle Variation of Global Mean Temperatures, 1991, Journal of Geophysical Research, Vol. 96, Nr. A7, 045-11,055

Bougher, S. W., S. Engel, R. G. Roble, and B. Foster, Comparative terrestrial planet thermospheres: 3. Solar cycle variation of global structure and winds at solstices, 2000, J. Geophys. Res., 105, 17,669–17,689.

Bougher, S. W., T. E. Cravens, J. Grebowsky, J. Luhmann, The aeronomy of Mars: Characterization by MAVEN of the upper atmosphere reservoir that regulates volatile escape. 2014, Space Sci. Rev. doi: 10.1007/s11214-014-0053-7

Bougher, S. W., K. J. Roeten, K. Olsen, P. R. Mahaffy, M. Benna, M. Elrod et al., The structure and variability of Mars dayside thermosphere from MAVEN/NGIMS and IUVS measurements: Seasonal and solar activity trends in scale heights and temperatures, 2017, J. Geophys. Res. Space Physics,122, 1296–1313,doi:10.1002/2016JA023454

Chaufray, J. Y., J. Deighan, M. S. Chaffin, N. M. Schneider, W. E. McClintock, A. I. F. Stewart et al., Study of the Martian cold oxygen corona from the O I 130.4 nm by IUVS/MAVEN, 2015, Geophys. Res. Lett., 42, 9031–9039, doi:10.1002/ 2015GL065341.

Chaufray, J. Y., F. Leblanc, E. Quémerais, and J. L. Bertaux, Martian oxygen density at the exobase deduced from O I 130.4-nm observations by Spectroscopy for the Investigation of the Characteristics of the Atmosphere of Mars on Mars Express, 2009, J. Geophys. Res., 114, E02006, doi:10.1029/2008JE003130.

Curdt, W.; Brekke, P.; Feldman, U.; Wilhelm, K.; Dwivedi, B. N.; Schühle, U.; Lemaire, P., The SUMER spectral atlas of solar-disk features, 2001, Astronomy and Astrophysics, v.375, p.591-613

Deighan, J., M. S. Chaffin, J. Y. Chaufray, A. I. F. Stewart, N. M. Schneider, S. K. Jain et al., MAVEN IUVS observation of the hot oxygen corona at Mars, 2015, Geophys. Res. Lett., 42,9009–9014, doi:10.1002/2015GL065487.

Donahue, T. M., Upper Atmosphere and Ionosphere of Mars, 1966, Science, 152(3723), doi: 10.1126/science.152.3723.763

Eparvier, F. G., Chamberlin, P. C., Woods, T. N., and Thiemann, E. M. B., The solar extreme ultraviolet monitor for MAVEN, 2015, Space Science Reviews, 195(1-4), 293-301.

Forget, F., Hourdin, F., Fournier, R., Hourdin, C., Talagrand, O., Collins, M., et al., Improved general circulation models of the Martian atmosphere from the surface to above 80 km, 1999, Journal of Geophysical Research: Planets, 104(E10), 24155-24175.

Fox, J. L. and A. Dalgarno, Ionization, Luminosity, and Heating of the Upper Atmosphere of Mars, 1979, Journal of Geophysical Research, 84, A12

Fox, J. L., A. S. Johnson, S. G. Ard, N. S. Shuman, and A. A. Viggiano, Photochemical determination of O densities in the Martian thermosphere: Effect of a revised rate coefficient, 2017, Geophysical Research Letters, 44, 8099–8106, doi:10.1002/2017GL074562.

E. P. Gentieu and J. E. Mentall, Cross sections for production of the CO(A1Π–X1Σ) Fourth Positive band system and O(3S) by photodissociation of CO2, 1973, J. Chem. Phys. 58, 4803, https://doi.org/10.1063/1.1679063

Gérard, J.-C., B. Hubert, V. I. Shematovich, D. V. Bisikalo, G. R. Gladstone, The Venus ultraviolet oxygen dayglow and aurora: Model comparison with observations, 2008, Planetary and Space Science, 56(3-4), https://doi.org/10.1016/j.pss.2007.11.008

Gkouvelis, L., J.-C. Gérard, B. Ritter, B. Hubert, N. Schneider, S. Jain, The O(1S) 297.2 nm dayglow emission: a tracer of CO2 density variations in the Martian lower thermosphere, 2018, Journal of Geophysical Research: Planets, DOI: 10.1029/2018JE005709

Gladstone, G. R., Radiative transfer of resonance lines with internal sources, 1985, J. Quant. Spectrosc. Radiat. Trans. 33, 453–458.

Gladstone, G. R., UV resonance line dayglow emissions on Earth and Jupiter, 1988, Journal of Geophysical Research – Space Physics, 93, A12,623-14,630

Gladstone, G. R., Solar OI 1304 A triplet line profiles, 1992, J. Geophys. Res. 97, 19125–19519.

González-Galindo, F., Forget, F., López - Valverde, M. A., Angelats i Coll, M., and Millour, E., A ground - to - exosphere Martian general circulation model: 1. Seasonal, diurnal, and solar cycle variation of thermospheric temperatures. 2009, Journal of Geophysical Research: Planets, 114(E4).

González-Galindo, F., López-Valverde, M. A., Forget, F., García-Comas, M., Millour, E., and Montabone, L., Variability of the Martian thermosphere during eight Martian years as simulated by a ground-to-exosphere global circulation model, 2015, Journal of Geophysical Research: Planets, 120(11), 2020-2035.

Green, A. E. S. and R. S. Stolarski, Analytic models of electron impact excitation cross sections, 1972, Journal of Atmospheric and Terrestrial Physics, 34, 1703-1717

Hanson W. B., S. Sanatani and D. R. Zuccaro, The Martian Ionosphere as Observed by the Viking Retarding Potential Analyzers, 1977, Journal of Geophysical Research, 82(28)

Hubert, B., J.-C. Gérard, J. Gustin, V. I. Shematovich, D. V. Bisikalo, A. I. Stewart, G. R. Gladstone, UVIS observations of the FUV OI and CO 4P Venus dayglow during the Cassini flyby, 2010, Icarus, 207, 549-557

Hubert, B., J.-C. Gérard, V. I. Shematovich, D. V. Bisikalo, S. Chakrabarti, G. R. Gladstone, Nonthermal radiative transfer of oxygen 98.9 nm ultraviolet emission : solving an old mystery, 2015, Journal of Geophysical Research - Space Physics, 120, doi:10.1002/2014JA020835, 2015.

Huebner, W.F., Keady, J.J., Lyon, S.P., Solar photo rates for planetary atmospheres and atmospheric pollutants, 1992, Astrophys. Space Sci. 195, 1–289.

Itikawa, Cross Sections for Electron Collisions With Carbon Dioxide, 2002, Journal of Physical and Chemical Reference Data 31, 749 (2002); doi: 10.1063/1.1481879

Jackman, C. H., R. H. Garvey, and A. E. S. Green, Electron impact on atmospheric gases I: updated cross sections, 1977, Journal of Geophysical Research, 82(32)

Jain, S. K., A. I . F. Stewart, N. M. Schneider, J. Deighan, A. Stiepen, J. S. Evans et al., The structure and variability of Mars upper atmosphere as seen in MAVEN/IUVS dayglow observations, 2015, Geophysical Research Letters, 42, 9023–9030, doi:10.1002/2015GL065419

Jakosky, B. M., R. P. Lin, J. M. Grebowsky, J. G. Luhmann, D. F. Mitchell, G. Beutelschies et al., The Mars Atmosphere and Volatile EvolutioN (MAVEN) mission, 2015, Space Sci. Rev., 195(1-4), doi:10.1007/s11214-015-0139-x.

Johnson, P. V., I. Kanik, D. E. Shemansky, x. Liu, Electron-impact cross sections of atomic oxygen, 2003, Journal of Physics B: Atomic, Moleculat and Optical Physics, 36, 3203-3218

Leblanc, F., J. Y. Chaufray, J. Lilensten, O. Witasse, and J.-L. Bertaux, Martian dayglow as seen by the SPICAM UV spectrograph on Mars Express, 2006, Journal of Geophysical Research, 111, E09S11, doi:10.1029/2005JE002664.

Lee, Y., M. R. Combi, V. Tenishev, S. W. Bougher, and R. J. Lillis, Hot oxygen corona at Mars and the photochemical escape of oxygen: Improved description of the thermosphere, ionosphere, and exosphere, 2014, J. Geophys. Res. Planets, 120,1880–1892, doi:10.1002/2015JE004890.

Mahaffy, P. R., Benna, M., King, T., Harpold, D. N., Arvey, R., Barciniak, M. et al., The neutral gas and ion mass spectrometer on the Mars atmosphere and volatile evolution mission, 2015, Space Science Reviews, 195(1-4), 49-73.

Mason, N. J., Measurement of the lifetime of metastable species by electron impact dissociation of molecules, Measurement Science and Technology, 1(7), 596-600, 1990, doi:10.1088/0957-0233/1/7/009

McClintock, W. E., Schneider, N. M., Holsclaw, G. M., Clarke, J. T., Hoskins, A. C., Stewart, I. et al., The imaging ultraviolet spectrograph (IUVS) for the MAVEN mission, 2015, Space Science Reviews, 195(1-4), 75-124.

McElroy, M. B., The Upper Atmosphere of Mars, 1967, Astrophysical Journal, vol. 150, p.1125 1967 ApJ...150.1125M

Millour, E., Forget, F., González-Galindo, F., Spiga, A., et al., 2009. The Mars Climate Database (version 4.3). SAE Technical Paper 2009-01-2395. http://dx.doi.org/10.4271/2009-01-2395.

Millour, E., F. Forget, A. Spiga, M. Vals, V. Zakharov, T. Navarro et al., The Mars Climate Database (MCD version 5.3), 2017, In EGU General Assembly Conference Abstracts (Vol. 19, p. 12247).

Montabone, L., F. Forget, E. Millour, R. J. Wilson, S. R. Lewis, B. Cantor et al., Eight-year Climatology of Dust Optical Depth on Mars, 2015, Icarus, doi: http://dx.doi.org/10.1016/j.icarus.2014.12.034

Mumma, M. J., E. J. Stone, W. L. Borst, and E. C. Zipf, Dissociative Excitation of Vacuum Ultraviolet Emission Features by Electron Impact on Molecular Gases. III. CO_2, 1972, J. Chem. Phys. 57, 6, doi.org/10.1063/1.1678019

Nier, A. O., and M. B. McElroy, Composition and structure of Mars' upper atmosphere results from the neutral mass spectrometers on Viking 1 and 2, 1977, J. Geophys. Res., 82, 4341–4349, doi:10.1029/JS082i028p04341.

Shematovich, V. I., D. V. Bisikalo, J.-C. Gérard, C. Cox, S. W. Bougher, and F. Leblanc, Monte Carlo model of electron transport for the calculation of Mars dayglow emissions, 2008, J. Geophys. Res., 113, E02011, doi:10.1029/2007JE002938.

Stevens, M. H., J. Gustin, J. M. Ajello, J. S. Evans, R. R. Meier, A. J. Kochenash et al., The production of Titan's ultraviolet nitrogen airglow, 2011, Journal of Geophysical Research – Space Physics, 116, A05304, doi:10.1029/2010JA016284.

Steward, A. I., Mariner 6 and 7 Ultraviolet Spectrometer Experiment: Implications of CO_2^+, CO, and O Airglow, 1972, Journal of Geophysical Research, 77(1)

Steward, A. I. F., M. J. Alexander, R. R. Meier, L. J. Paxton, S. W. Bougher and C. G. Fesen, Atomic Oxygen in the Martian Thermosphere, 1992, Journal of Geophysical Research, 97(A1), 91-102

Stone E. J. and E. C. Zipf, Electron-impact excitation of the 3S0 and 5S0 states of atomic oxygen, 1974, Journal of Chemical Physics, 60, doi: 10.1063/1.1680894

Stone, S. W., R. V. Yelle, M. Benna ,M. K. Elrod and P. R. Mahaffy, Thermal structure of the Martian upper atmosphere from MAVEN/NGIMS, 2018, Journal of Geophysical Research: Planets, 123, 2842–2867, https://doi.org/10.1029/2018JE005559

Strickland, D. J., G. E. Thomas and P. R. Sparks, Mariner 6 and 7 Ultraviolet Spectrometer Experiment: Analysis of the OI 1304- and 1356-A Emissions, 1972, Journal of Geophysical Research, 77(22)

Strickland, D. J., A. I. Stewart, C. A. Barth and C. W. Hord, Mariner 9 Ultraviolet Spectrometer Experiment: Mars Atomic Oxygen 1304-A Emission, 1973, Journal of Geophysical Research, 78(22)

Tayal, S. S. and O. Zatsarinny, B-spline R-matrix-with-pseudostates approach for excitation and ionization of atomic oxygen by electron collisions, 2016, Physical Review, A94, 042707, doi: 10.1103/PhysRevA.94.042707

Thiemann, E., Chamberlin, P. C., Eparvier, F. G., Templeman, B., Woods, T. N., Bougher, S.W., and Jakosky, B. M., The MAVEN EUVM model of solar spectral irradiance variability at Mars: Algorithms and results, 2017, Journal of Geophysical Research: Space Physics, 122(3), 2748-2767.

Thomas, G. E., Neutral Composition of the Upper Atmosphere of Mars as Determined from the Mariner UV Spectrometer Experiments, 1971, Journal of the Atmospheric Sciences, 28

Venot, O., Y. Bénilan, N. Fray, M.-C. Gazeau, F. Lefèvre, Et. Es-sebbar, E. et al., VUV-absorption cross section of carbon dioxide from 150 to 800 K and applications to warm exoplanetary atmospheres. Astronomy & Astrophysics, 609, A34.

Woods, T. N., M. Snow, J. Harder, G. Chapman, A. Cookson, A Different View of Solar Spectral Irradiance Variations: Modeling Total Energy over Six-Month Intervals, 2015, Solar Physics, DOI 10.1007/s11207-015-0766-0

Zipf, E. C., and P. W. Erdman, Electron Impact Excitation of Atomic Oxygen: Revised Cross Section, 1985, Journal of Geophysical Research, 90(A11), 11,087-11,090

Table 1: Parameters of the two datasets shown in Figure 5 and Figure 7. For L_S, LT, SZA and latitude the mean values of the respective sample and their standard deviation within that sample are given. Additionally, the maximum fitted brightness (B_{max}), the corresponding altitude (Z_{max}) and the scale heights (H) are listed. The values in parentheses refer to the model results.

	MY 32	**MY 33**
Solar longitude	350.02 ± 0.91	350.00 ± 0.42
Local time	9.76 ± 0.08	14.14 ± 0.10
SZA	35.29 ± 1.54	33.66 ± 1.09
Latitude	-16.68° ± 2.48	-15.21° ± 3.35
Number of scans	13	17
Orbits	1275 – 1303	4920 – 4938
Earth date	27/05/2015 – 01/06/2015	13/04/2017 – 16/04/2017
B_{max} 130.4 nm data (model)	1.15 ± 0.08 kR (1.10 kR)	0.80 ± 0.6 kR (0.83 kR)
B_{max} 135.6 nm data (model)	0.68 ± 0.09 kR (0.65 kR)	0.37 ± 0.04 kR (0.35 kR)
Z_{max} 130.4 nm data (model)	128 ± 1 km (128 km)	131 ± 1 km (126 km)
Z_{max} 135.6 nm data (model)	126 ± 1 km (129 km)	128 ± 1 km (125 km)
H 130.4 nm data (model)	199 km (155 km)	258 km (133 km)
H 135.6 nm data (model)	24 km (23 km)	24 km (20 km)

Figure 1: (a) MAVEN/IUVS FUV mean limb spectrum: average of 19 individual scans recorded between 120 and 140 km altitude. (b) the same 19 limb profiles at 130.4 nm (blue on the right) and at 135.6 nm (red on the left). The dots indicate the maximum intensity between 110 and 155 km tangent point (TP) altitude for each individual profile. The data has been taken in MY 32 at L_S=309°, between orbits 885 and 890, around 16h local time in an SZA interval of 56°-63° and a latitude interval of -6° to 10°.

Figure 2: All data of 130.4 nm peak brightness versus orbit number, the three panels cover 60° latitude each, going from north (a) to south (c). The color code indicates local time (LT) intervals with the restriction of the SZA≤75°. Martian season (solar longitude) and Earth date are also indicated. Figure S1 shows the corresponding plot at 135.6 nm.

Figure 3: Distribution of peak intensity altitudes at 130.4 nm (a) and at 135.6 nm (b). The data are binned into intervals of 100 orbits and 5 km altitude.

Figure 4: (a) 130.4 nm (blue) and 135.6 nm (red) maximum brightness of each limb profile versus orbit number for all data with SZA<40°. (b) same as (a), but the brightness at 130.4 and 135.6 nm is normalized by the solar flux (see text). (c) 130.4 nm solar triplet flux (blue) and EUV integrated flux from 10-55 nm (red) from EUVM, and distance to Mars to Sun (black).

Figure 5: (a): Peak brightness at 130.4 nm versus peak brightness at 135.6 nm with a linear fit. Fit equation and correlation factor R are given. The two dataset discussed in Section 3.4 and after are shown as yellow triangles (MY 32) and blue filled circles (MY33, Table 1). (b): same as (a), but the brightness is normalized by the respective solar flux (F_{sol}). The reduced χ^2 of the linear fits are 92.3 and 4.3, respectively. (c) Peak brightness altitudes of individual limb scans at

135.6 nm line versus the peak brightness altitude at 130.4 nm in 5 km altitude bins. The grey line indicates the angle bisector.

Figure 6: Solar flux-normalized 130.4 nm intensities vs. SZA for latitude and L_S intervals.

Figure 7: IUVS limb profiles at 130.4 nm (blue, left) and at 135.6 nm (red, right) for the two datasets in MY 32 (top) and MY 33 (bottom). The mean profiles and their ±1-σ variability are shown by the data points with horizontal bars.

Figure 8: (a) Vertical density profiles of species related to oxygen photochemistry and (b) temperature profiles extracted from the MCD for the two conditions described in Table 1. The solid lines show the profiles for MY 32 and the dashed lines for MY 33.

Figure 9: Peak brightness (top row) and peak altitude (bottom row) at 130.4 nm (blue) and at 135.6 nm (red) in dependence of the oxygen (a, f), CO_2 (b, g) and all atmospheric components' (c, h) density, and the beak brightness in dependence of the isothermal temperature (T_{iso}) (d) of the solar flux (e). The filled circles indicate the IUVS dataset taken in MY 33 (Table 1).

Figure 10: Model-data comparison for the datasets from MY 32 (a) and MY 33 (b). The mean profiles from Figure 7 are plotted as points with horizontal variability bars reflecting the brightness variation within each dataset. The solid lines represent the total modeled brightness, the dashed lines the major and the dashed-dotted lines the minor contributor to the modeled brightness.

Figure 1.

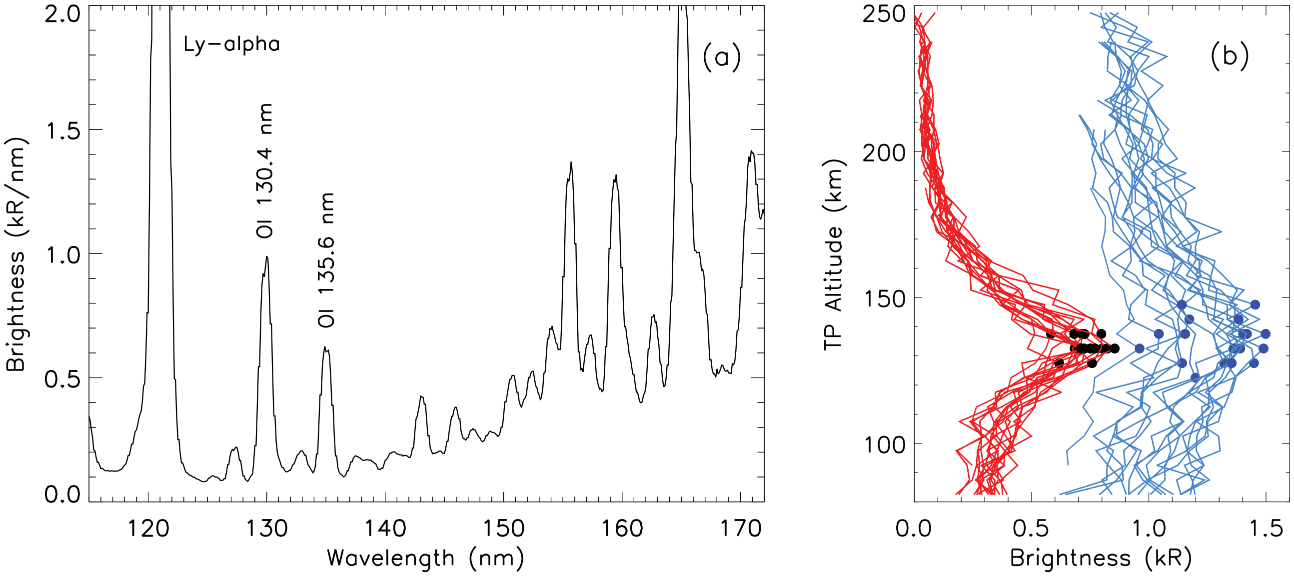
Ly−alpha
OI 130.4 nm
OI 135.6 nm
(a)
Brightness (kR/nm)
2.0
1.5
1.0
0.5
0.0
120
130
140
150
160
170
Wavelength (nm)
(b)
TP Altitude (km)
250
200
150
100
0.0
0.5
1.0
1.5
Brightness (kR)

Figure 2.

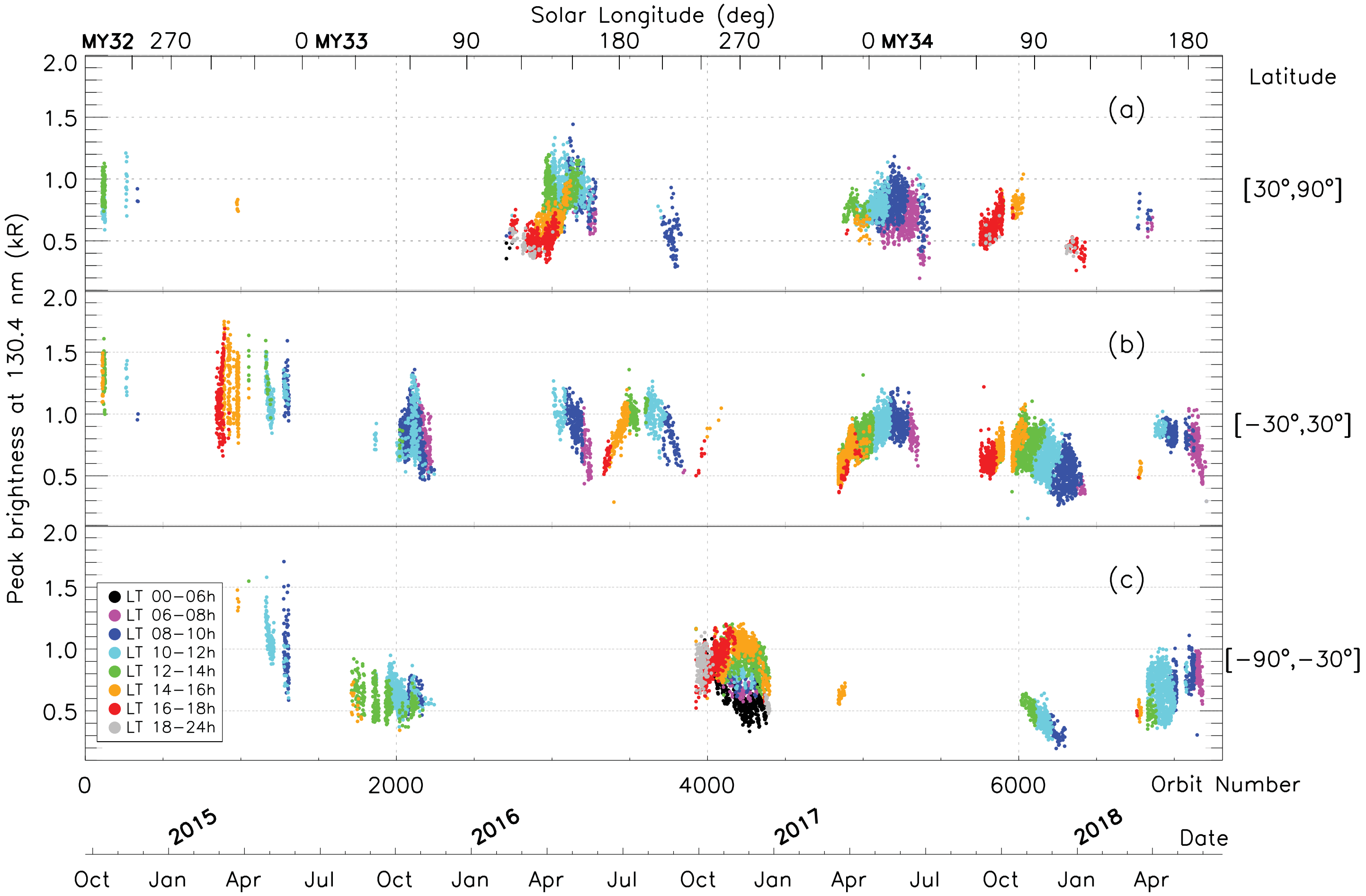
Solar Longitude (deg)
MY32 270
0 MY33
90
180
270
0 MY34
90
180
Latitude
(a)
[30°,90°]
(b)
[−30°,30°]
(c)
[−90°,−30°]
Peak brightness at 130.4 nm (kR)
2.0
1.5
1.0
0.5
● LT 00−06h
● LT 06−08h
● LT 08−10h
● LT 10−12h
● LT 12−14h
● LT 14−16h
● LT 16−18h
● LT 18−24h
0
2000
4000
6000
Orbit Number
2015
2016
2017
2018
Date
Oct
Jan
Apr
Jul
Oct
Jan
Apr
Jul
Oct
Jan
Apr
Jul
Oct
Jan
Apr

Figure 3.

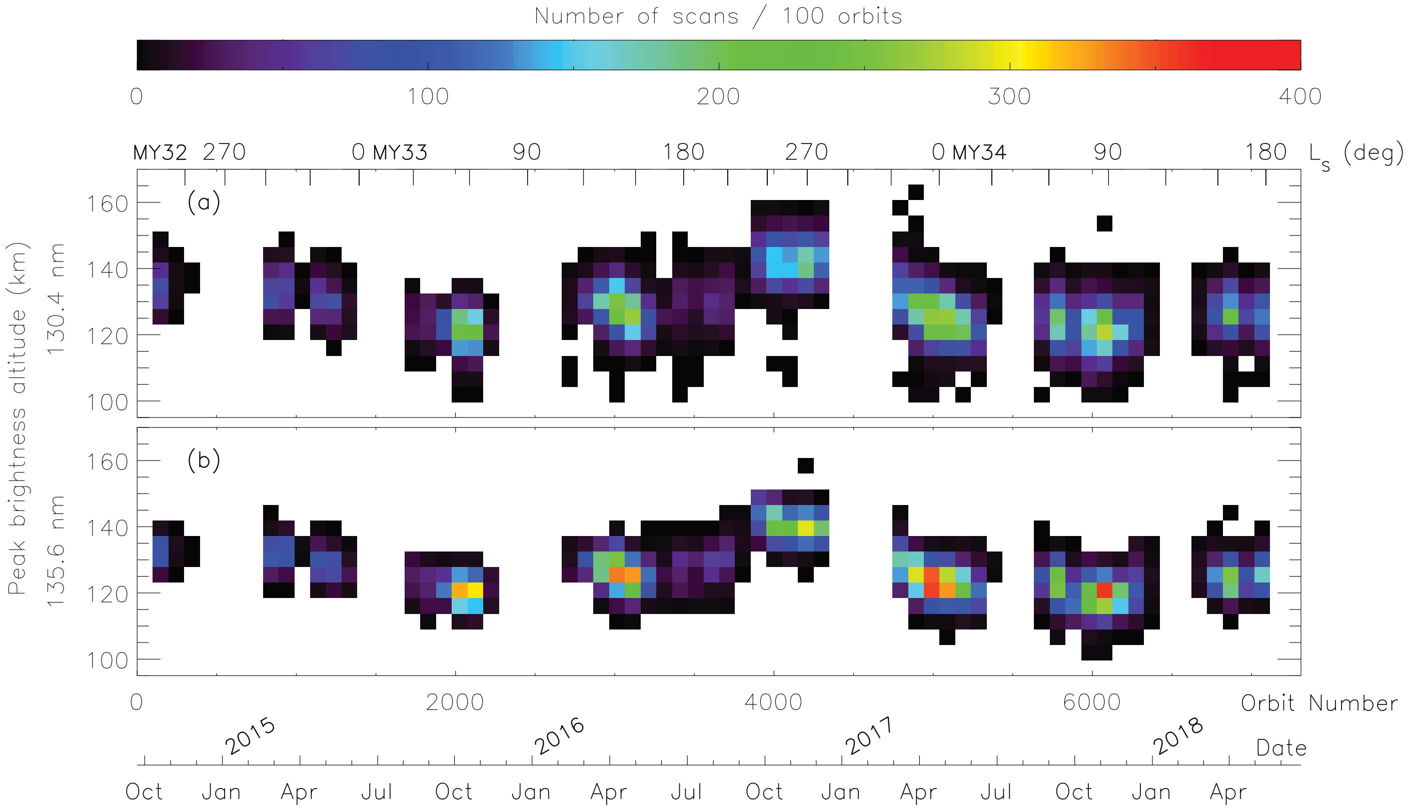
Number of scans / 100 orbits
0
100
200
300
400
MY32 270
0 MY33
90
180
270
0 MY34
90
180
L_s (deg)
Peak brightness altitude (km)
130.4 nm
135.6 nm
(a)
(b)
160
140
120
100
0
2000
4000
6000
Orbit Number
2015
2016
2017
2018
Date
Oct
Jan
Apr
Jul
Oct
Jan
Apr
Jul
Oct
Jan
Apr
Jul
Oct
Jan
Apr

Figure 4.

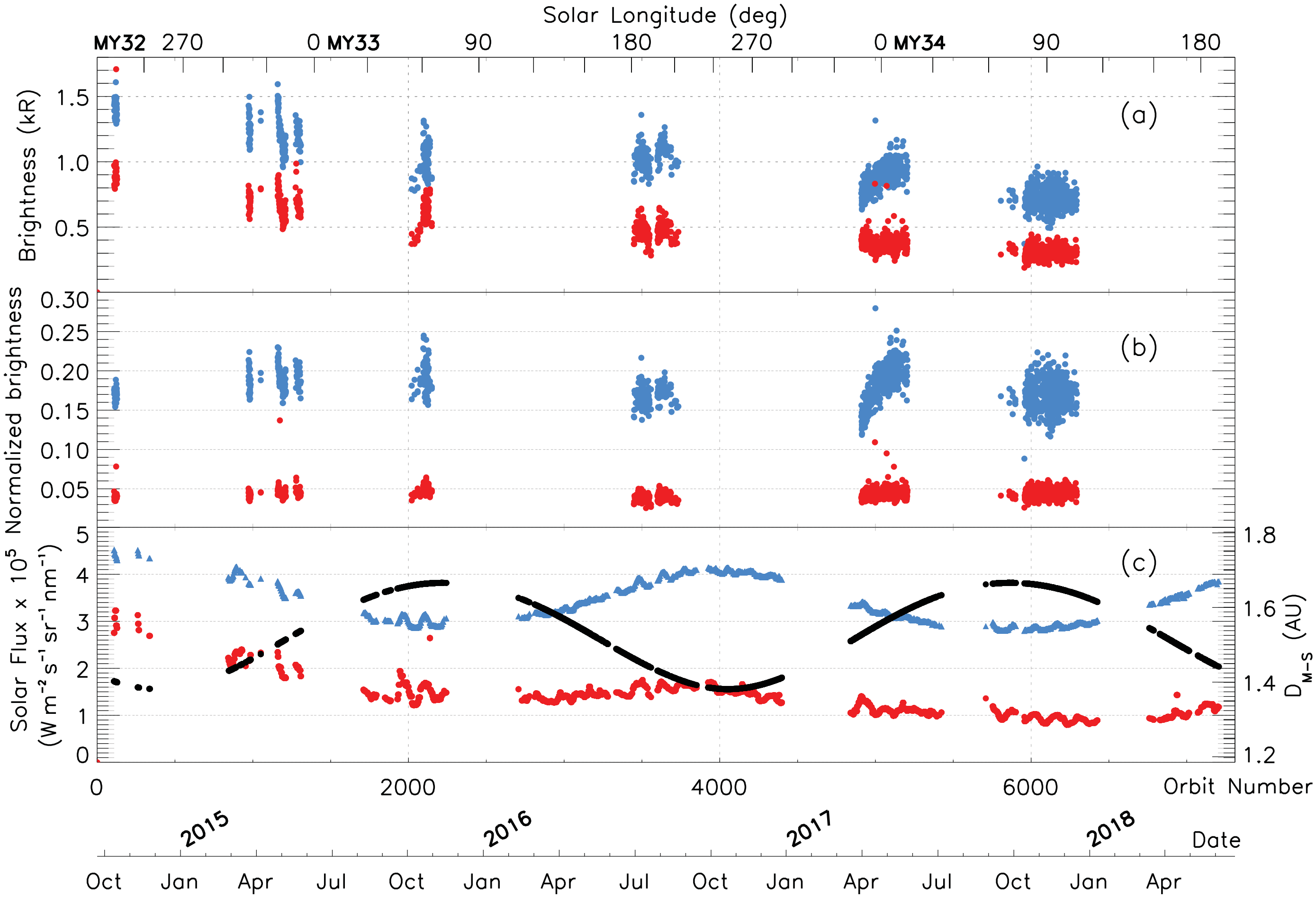
Solar Longitude (deg)
MY32
270
0
MY33
90
180
270
0
MY34
90
180
Brightness (kR)
1.5
1.0
0.5
(a)
Normalized brightness
0.30
0.25
0.20
0.15
0.10
0.05
(b)
Solar Flux x 10^5 ($W m^{-2} s^{-1} sr^{-1} nm^{-1}$)
5
4
3
2
1
0
(c)
1.8
1.6
1.4
1.2
D_{M-S} (AU)
0
2000
4000
6000
Orbit Number
2015
2016
2017
2018
Date
Oct
Jan
Apr
Jul
Oct
Jan
Apr
Jul
Oct
Jan
Apr
Jul
Oct
Jan
Apr

Figure 5.

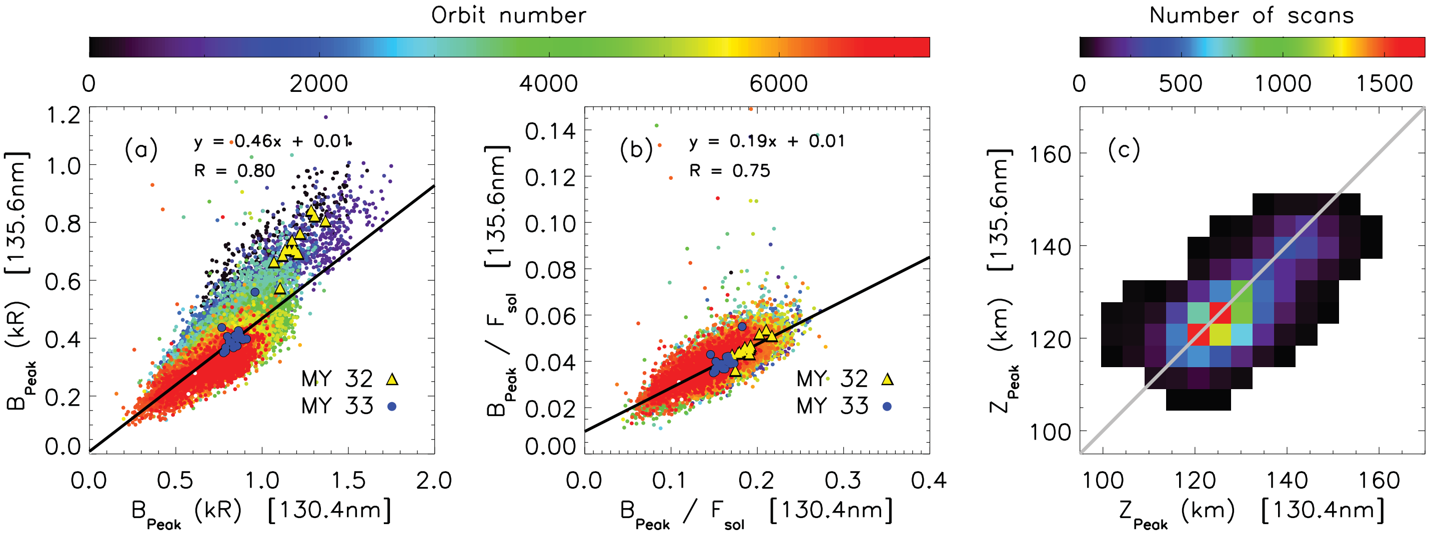
Orbit number
0
2000
4000
6000
Number of scans
0
500
1000
1500
(a)
y = 0.46x + 0.01
R = 0.80
MY 32
MY 33
B_{Peak} (kR) [135.6nm]
B_{Peak} (kR) [130.4nm]
0.0
0.2
0.4
0.6
0.8
1.0
1.2
0.0
0.5
1.0
1.5
2.0
(b)
y = 0.19x + 0.01
R = 0.75
MY 32
MY 33
B_{Peak} / F_{sol} [135.6nm]
B_{Peak} / F_{sol} [130.4nm]
0.00
0.02
0.04
0.06
0.08
0.10
0.12
0.14
0.0
0.1
0.2
0.3
0.4
(c)
Z_{Peak} (km) [135.6nm]
Z_{Peak} (km) [130.4nm]
100
120
140
160
100
120
140
160

Figure 6.

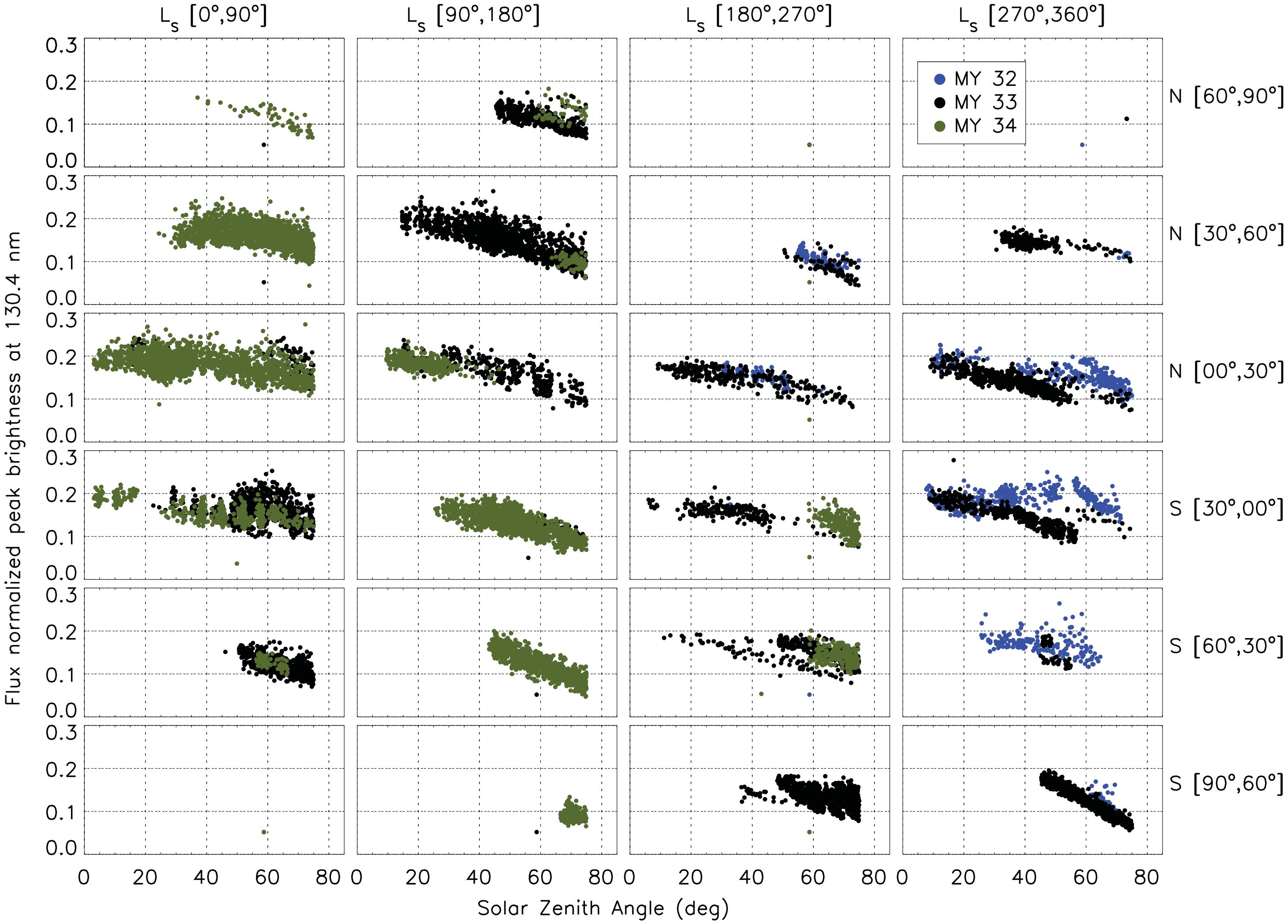

L_s [0°,90°]
L_s [90°,180°]
L_s [180°,270°]
L_s [270°,360°]
MY 32
MY 33
MY 34
N [60°,90°]
N [30°,60°]
N [00°,30°]
S [30°,00°]
S [60°,30°]
S [90°,60°]
Flux normalized peak brightness at 130.4 nm
0.0
0.1
0.2
0.3
0
20
40
60
80
Solar Zenith Angle (deg)

Figure 7.

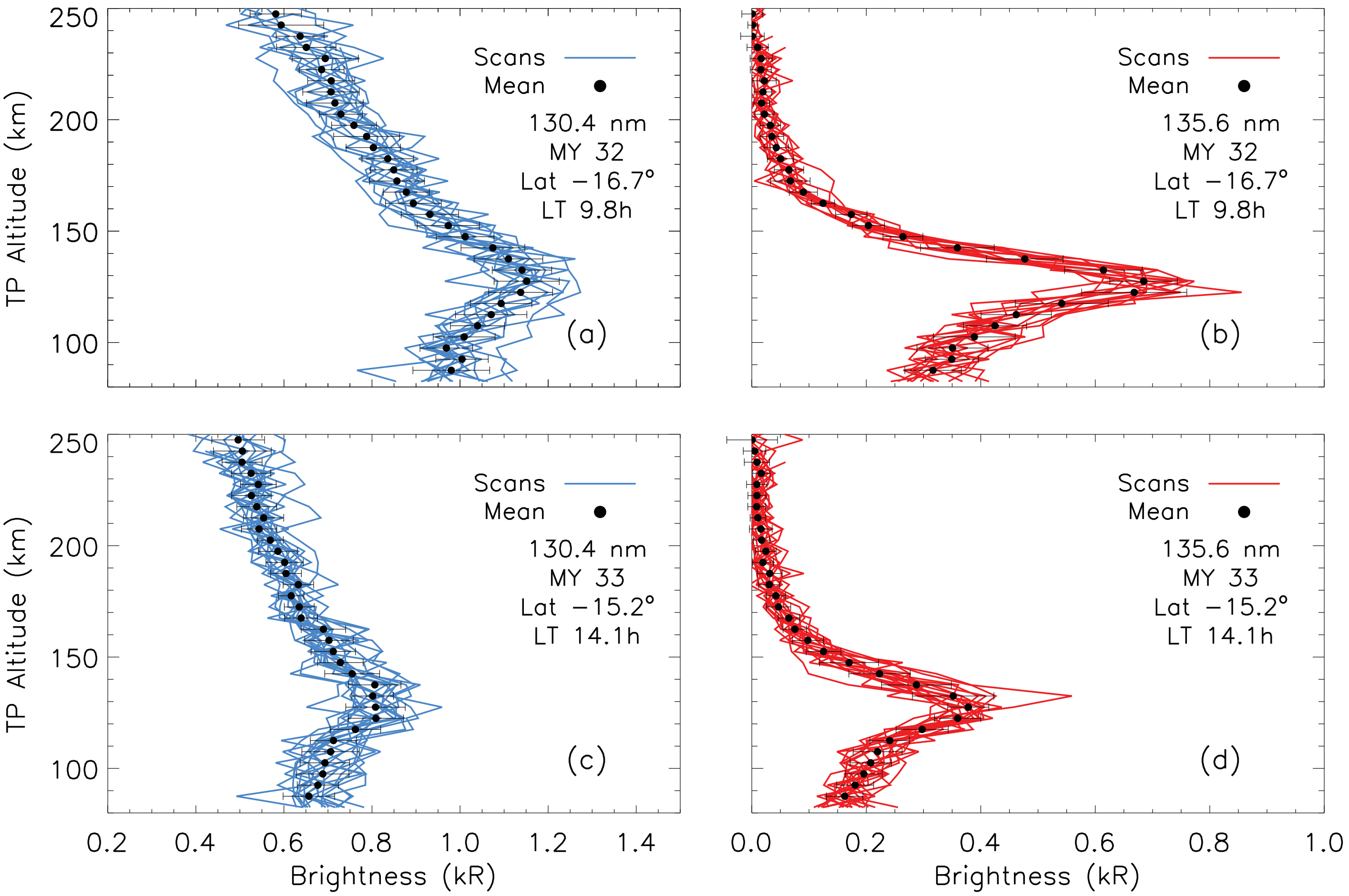
250
200
150
100
TP Altitude (km)
Scans
Mean
130.4 nm
MY 32
Lat −16.7°
LT 9.8h
(a)
135.6 nm
MY 32
Lat −16.7°
LT 9.8h
(b)
130.4 nm
MY 33
Lat −15.2°
LT 14.1h
(c)
135.6 nm
MY 33
Lat −15.2°
LT 14.1h
(d)
0.2
0.4
0.6
0.8
1.0
1.2
1.4
Brightness (kR)
0.0
0.2
0.4
0.6
0.8
1.0
Brightness (kR)

Figure 8.

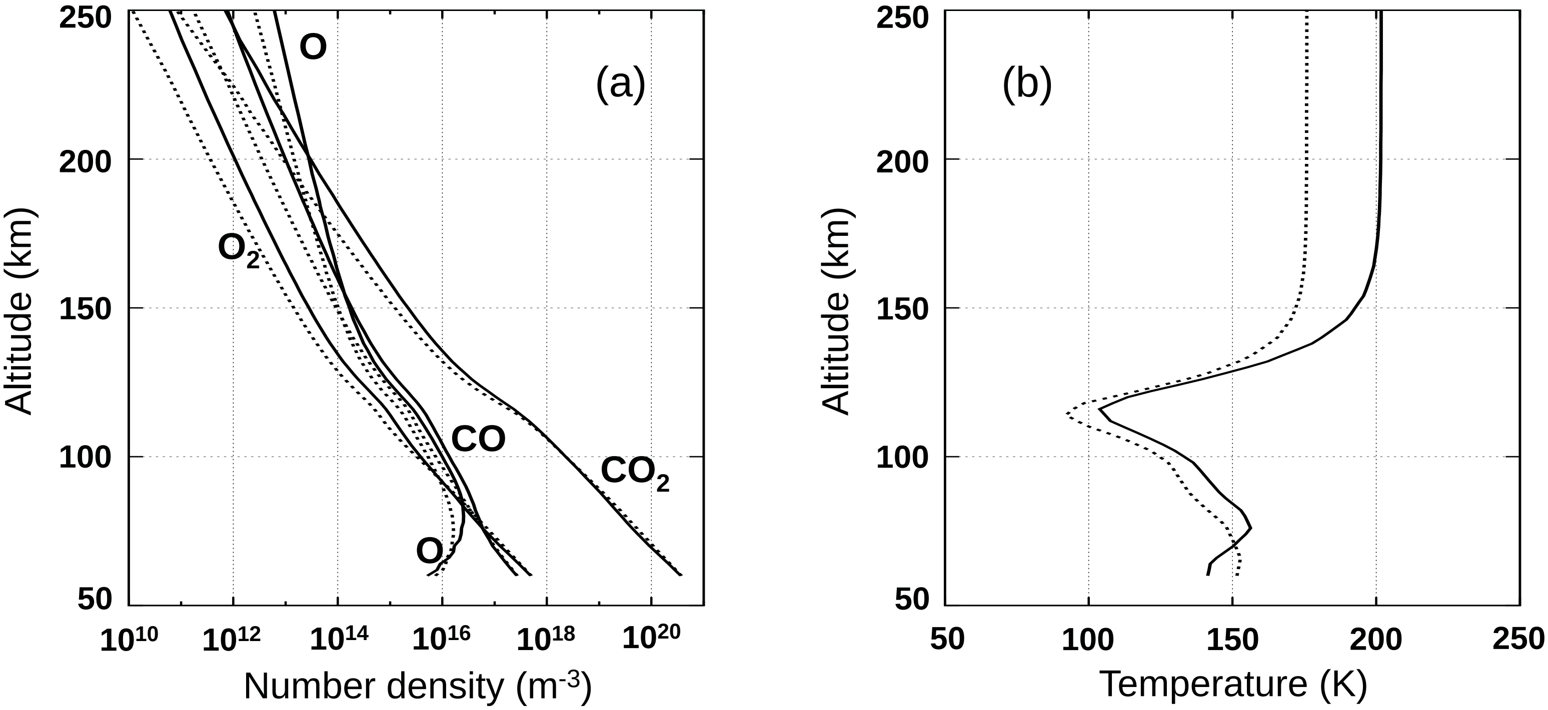

(a)
O
O$_2$
CO
CO$_2$
O
Altitude (km)
250
200
150
100
50
10^{10}
10^{12}
10^{14}
10^{16}
10^{18}
10^{20}
Number density (m^{-3})
(b)
Altitude (km)
250
200
150
100
50
50
100
150
200
250
Temperature (K)

Figure 9.

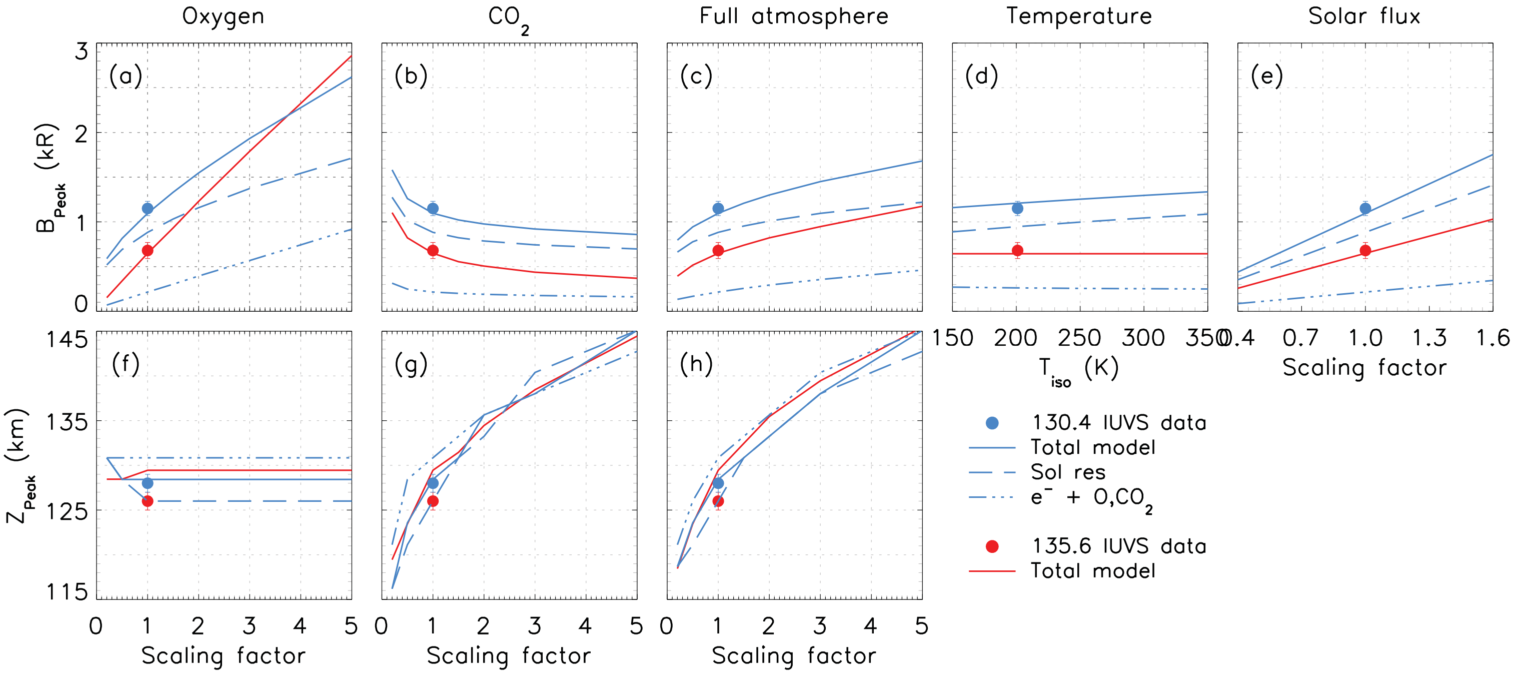

Oxygen
CO$_2$
Full atmosphere
Temperature
Solar flux
(a)
(b)
(c)
(d)
(e)
(f)
(g)
(h)
B$_{Peak}$ (kR)
Z$_{Peak}$ (km)
0
1
2
3
115
125
135
145
0
1
2
3
4
5
Scaling factor
150
200
250
300
350
T$_{iso}$ (K)
0.4
0.7
1.0
1.3
1.6
Scaling factor
130.4 IUVS data
Total model
Sol res
e$^-$ + O,CO$_2$
135.6 IUVS data
Total model

Figure 10.

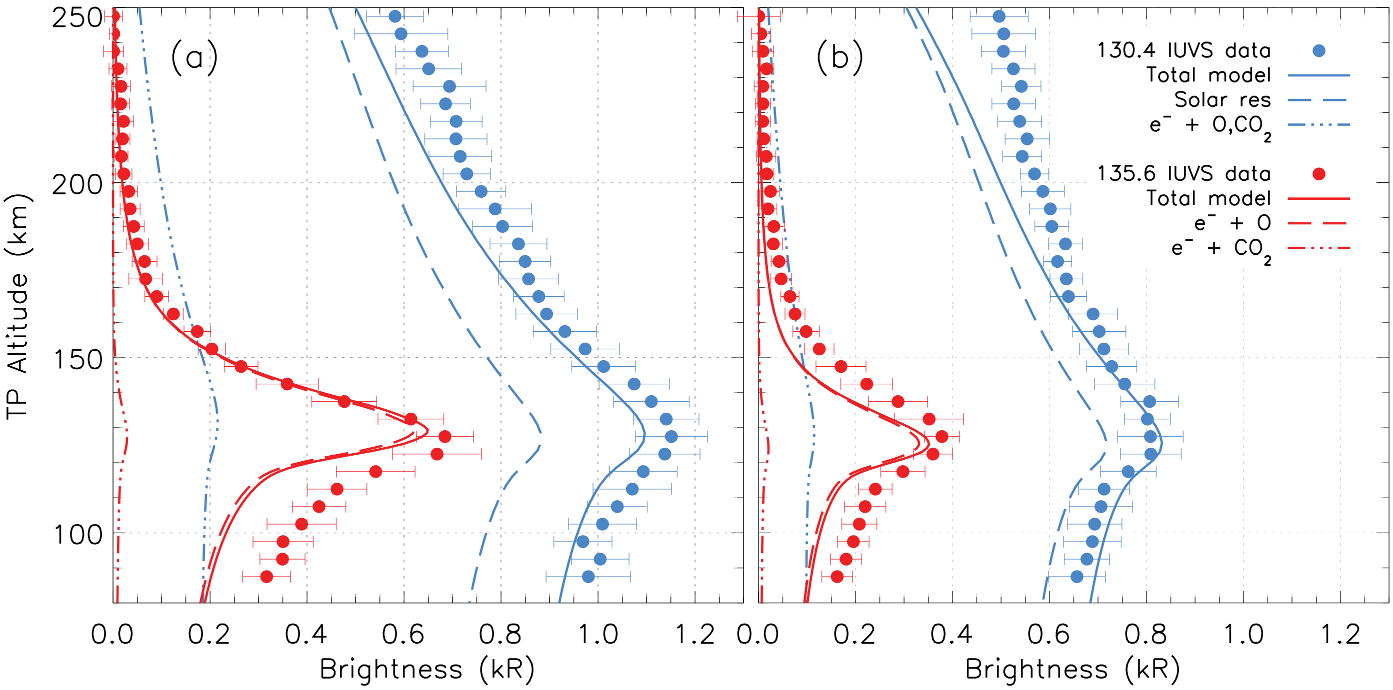
(a)
(b)
TP Altitude (km)
Brightness (kR)
250
200
150
100
0.0
0.2
0.4
0.6
0.8
1.0
1.2
130.4 IUVS data
Total model
Solar res
e^- + O,CO_2
135.6 IUVS data
Total model
e^- + O
e^- + CO_2